Nonlinear Dyn
https://doi.org/10.1007/s11071-025-10922-w

RESEARCH

Nonlinear experimental dynamics of a pentastable composite cantilever shell

Lukasz Kloda · Danyil Melnyk · Matteo Brunetti · Jerzy Warminski · Andrzej Mitura · Francesco Romeo

Received: 30 September 2024 / Accepted: 20 January 2025

Abstract A composite shell with conical geometry, featuring opposite curvatures in its free (undeformed) configuration, is studied. Prestress is applied by first flattening and then clamping one of the curved edges, leading to a morphing structure. The shell exhibits five distinct static equilibria, referred to as configurations **I**, **J**, **L**, **S**, and **I***. Based on experimental measurements and numerical models, the rich potential energy topology is qualitatively reconstructed. The linear dynamics of the cantilevered shell is investigated at first through various scenarios of kinematic excitation over a wide range of frequencies (up to 100 Hz). Frequency response curves, time series, phase portraits, Poincaré maps, fast Fourier transforms and largest Lyapunov exponents are used to investigate in-well, cross-well, and global nonlinear dynamics. Depending on the forcing amplitude and frequency, one-way and reversible snap-through is observed. The extensive experimental campaign allows to unveil the dynamic interplay among the observed five stable configurations.

Keywords Pentastable shell · Morphing structure · Snap-through effect · Cantilever shell · In/cross-well and global dynamics

L. Kloda (✉) · D. Melnyk · J. Warminski · A. Mitura
Department of Applied Mechanics, Lublin University of Technology, Nadbystrzycka 36, 20-618 Lublin, Poland
e-mail: l.kloda@pollub.pl

D. Melnyk
e-mail: danyil.melnyk@pollub.edu.pl

J. Warminski
e-mail: j.warminski@pollub.pl

A. Mitura
e-mail: a.mitura@pollub.pl

M. Brunetti
Polytechnic Department of Engineering and Architecture, University of Udine, via delle Scienze 206, 33100 Udine, Italy
e-mail: matteo.brunetti@uniud.it

F. Romeo
Department of Structural and Geotechnical Engineering, Sapienza University of Rome, Via Gramsci 53, 00197 Rome, Italy
e-mail: francesco.romeo@uniroma1.it

1 Introduction

In recent decades, multistable structures, especially composite laminates, have gained attention for their ability to move between different stable equilibrium points when properly actuated. These structures do not require external power to maintain a stable configuration, as they inherently sustain a self-balanced state. This property makes multistable structures suitable for use in morphing applications where the structure configuration must constantly adapt to changing operating conditions. Multistability has demonstrated unique advantages in various applications, including signal processing [1], energy harvesting [2,3], composite structures [4,5], metamaterials [6,7], micro- and nano-electromechanical systems (MEMS/NEMS) [8,9]. Bistable and multistable systems offer signifi-

Published online: 10 February 2025

cant benefits in a variety of applications. They improve energy harvesters by enhancing motion and power output, and increase the flexibility of composite structures and metamaterials, which is useful for aircraft, helicopter rotorcraft and robots. In addition, the nonlinearity of these systems provides a wide operating frequency bandwidth and maintains stable equilibrium configurations without external energy, making them ideal for designing reconfigurable structures such as soft robot arms and wind turbine blades. Multistable structures in particular provide more stable states and improved energy output at low excitation levels in comparison to bistable ones [10].

Mechanical multistability was firstly discovered several decades ago by [11] for asymmetrical composite laminates, in which the curing process, after the production procedure, causes thermal permanent stresses. Subsequent research has advanced the development of multistable composites using thermally induced laminates by exploring methods such as discontinuous [12] and continuous [13] and [14] assembly, tailored laminates [15], and tailored fiber-reinforced polymer (FRP) laminates [16], with varying layer stacking sequences (e.g., asymmetric, antisymmetric [0n, 90n], [−45n, 45n], or symmetric [0n, 0n] configurations). However, the stable equilibrium configurations obtained by this method are very sensitive to temperature but less affected by moisture. In works [17] and [18] were found that increased humidity significantly changes the laminate curvature and reduces the snap-through load while maintaining bistability. Prestressing techniques has been introduced to reduce hydrothermal variability in composite structures and improve shape control. Prestressed laminates, both flat [19] and curved [20], can achieve bistability, which contributes to increased strength and stress management. Another approach to achieve multistability involves using ferromagnetic forces, such as a cantilevered beam with a magnetic tip for magnetic repulsion [21] or attraction [22], or by integrating a magnetorheological elastomer with a composite shell [23]. Multistability can be caused by a specific construction such as spring-mass system proposed in [24].

In recent years bistable composite shells with initial nonlinear geometry gained high demand. Designing orthotropic materials with an initial curvature eliminate hydrothermal instability and achieve bistability or multistability without prestressing. Cylindrical shells can achieve bistability using either prestressed isotropic materials [20] or anisotropic materials without stress [25]. Later modifications to these models demonstrated that bistability depends on the initial Gaussian curvature, with isotropic shells requiring positive curvature and orthotropic shells achieving bistability with either positive or negative curvature [26].

Several techniques have been employed to achieve the snap-through effect. To maximize the kinetic energy during snap-through effect, different geometric configuration and boundary conditions were considered: by applying a vertical force to the center of the laminate supported at four points near a corners [27] or excite it with harmonic oscillations such as proposed in [28]; by exciting the foundation being a boundary condition, placed in the middle of cylindrical shell, near the vicinity of resonant frequency [29,30]; by blocking the middle point of double-curved shell and applying forces to the opposite edges such as shown in [31], this specific geometry allows to obtain three stable configurations of the structure a specific geometry first proposed by [32]; another solution was purposed in [33] by linking multiple bi-stable composite patches into a grid formation; due to peculiar design limitations and difficulties in [34] investigated a non-cylindrical shell on terms of multistability; several researchers have considered cantilever boundary conditions of both edges such as in [35] and clamping one end of shell with pseudo-conical initial geometry such as [36] and [37], where two types of shells' initial geometry were analyzed: shell A (initial curvatures with the same signs), shell B (initial curvatures with opposite signs). These works were extended in paper [38], where shells A and B were dedicated to finite element analysis (FEA) and for the first time shell B was produced, these shells exhibit two and four significantly different stable configurations, respectively. In the work [39] bistable shell A was dedicated for nonlinear dynamics tests and was extended in [40] in terms of experimental energy harvesting and purposing new material properties and aspect ratio. The asymmetry of the clamped stable states is controlled by the curvature of the stress-free configuration of the shell. Studies have shown that a significant difference between stable shell shapes increases the generation of kinetic energy levels that are typically not observable with symmetric stable shapes.

Despite the extensive literature on multistable structures, including their geometry, construction, and mechanical properties, research on multistable composite shells primarily focuses on structures with two slightly different stable configurations. Moreover, there is a lack of comprehensive experimental analysis of composite cantilever shells with piezoelectric overlays. Previous work [38] investigated a quad-stable composite shell with opposite curvatures and proposed a numerical model. Another study [39] examined the dynamics of a bistable shell with the same curvatures' (called shell-A) signs exhibiting significantly different stable equilibria. This paper aims to extend these studies by investigating a quad-stable shell with new material properties and thickness, both experimentally and numerically, and comparing the results. It seeks to observe the snap-through effect in response on harmonic excitation in a real composite shell prototype, considering manufacturing imperfections, non-perfect boundary conditions and ply-stack angles that are very difficult to model. Moreover, the study aims to explore all possible transitions between stable configurations, to identify all types of motions, which exhibit during snap-through motion and resonance response for all stable configurations, to select which ones are most effective candidates for energy harvesting from vibration. The main advantage of this investigation, in contrast to former study, is that the monolithic shell features five distinctly different stable configurations.

2 Static equilibria of shell with opposite conical curvatures

Let us reconsider a family of pseudoconical shells described in the three-dimensional $x_1x_2x_3$ coordinate system by Eq. 1. Setting the cantilever length of the shell to $L_1 = 0.45$ m and its width to $L_2 = 0.15$ m, a length to width ratio 3 : 1 is adopted. The coefficients r_0 and r_f denote the geometry with either the same curvatures shell **A** when r_0 and r_f have matching signs, or opposite curvatures shell **B** when parameters r_0 and r_f have opposite signs. Dynamics of composite shell **A** have been investigated in [39] and then extended for energy harvesting purposes in [40]. Now, we focus on the shell **B** with radii $r_0 = 0.114$ m and $r_f = -0.07$ m, in which four stable equilibria have been detected [38]. The geometry for the given set of parameters is shown in Fig. 1a. The original composite from which the structure was created, has been revised by changing only the lamina to reduce the system's stiffness. This revision aimed to lower natural frequencies and facilitate the transition between equilibria by significantly shallowing the potential wells, or more precisely, reducing the energy barriers required to transfer between states. Parameters of substituted material are listed in Table 1, while the prototype in a free configuration is presented in Fig. 1c.

$$w_0(x_1, x_2) = \left[\frac{1}{r_0} + \left(\frac{1}{r_f} - \frac{1}{r_0}\right)\frac{x_1}{L_1}\right]\frac{x_2^2}{2} \tag{1}$$

Introducing initial stresses at the clamp edge, the structure deforms to a configuration **I**, presented in Fig. 2a. Numerical simulations show that this configuration corresponds to $U_I = 160.7$ mJ stored strain energy. The deformation field can be divided into two sub-regions, a first, near-boundary region between the gripping part and the reference dashed gray line, where the transverse curvature changes from positive to negative (in the rest reference configuration it is located at $x_1/L_1 = 0.38$ while in configuration **I** shifts to 1/3rd of the shell's length in configuration **I**), and a second region, located between the curvature transition line and the free end of the shell. Both regions exhibit bistable properties, and considering the 2^2 possible combinations, the structure exhibits four equilibria. Therefore, in order to jump (snap-through) from configuration **I** to the configuration **J** presented in Fig. 2b, work must be done to "straighten" the free edge. This causes the system to snap into a new potential well, for which the stored strain energy $U_J = 470.5$ mJ is higher than the reference configuration **I**. In the second scenario, starting again from configuration **I**, work is done by lifting the end of the shell until the near-boundary segment jumps from the initial curvature into an almost straight line, while the end of the shell remains curved. The new configuration, labelled **L**, is shown in Fig. 2c and corresponds to a state with the lowest strain energy $U_L = 146.7$ mJ. Another examined equilibrium is configuration **S**, which is obtained by simultaneous falttening of the transversal curvature of the first and second regions, see Fig. 2d. This state exhibits the highest level of stored elastic energy due to the material strain of about $U_S = 485.3$ mJ. The four stable configurations **I**, **J**, **L** and **S** were captured in numerical finite element simulations performed in Abaqus_CAE© commercial software, as shown in Fig. 2. For more details on numerical simulations procedure we refer to [38].

Figure 2e shows the last equilibrium configuration observed only in experimental tests and not predicted by the numerical model. It is very similar to configura-

Table 1 Mechanical properties of the lamina NTPT 513/HR40/50GSM/35%/300 mm: original research from the tensile tests (TT) and accepted for finite element model (FEM)

	E_1 MPa	E_2 MPa	ν_{12} –	G_{12} MPa	G_{13} MPa	G_{23} MPa	ρ g/cm^3
TT	214621	8491	0.246	10690	10690	1000	1.287
FEM	220000	8491	0.246	10690	10690	1000	1.747

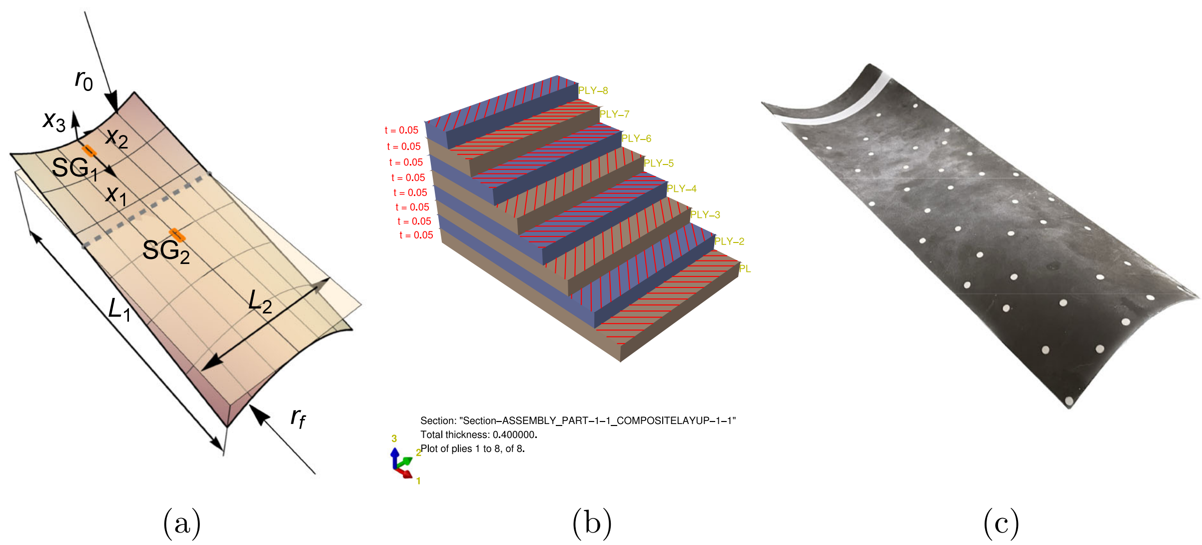

Fig. 1 Rest reference configuration of composite shell **B**: **a** mathematical model with indicated geometrical parameters, **b** composite sequence map $[45/-45_2/45/-45/45_2/-45]^T$ and **c** stress-free shell prototyped after autoclave process. Location of strain gauges SG_1 and SG_2 embedded at bottom surface are indicated in orange

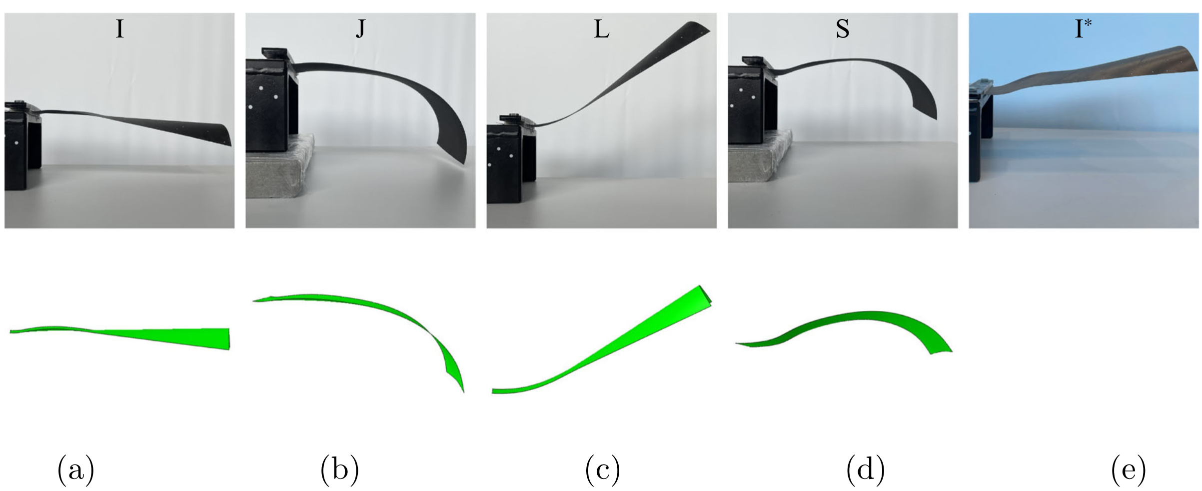

Fig. 2 Static equilibria of composite shell with pre-stresses at boundary conditions: **a** I-shape **b** J-shape **c** L-shape, **d** S-shape and **e** I*-Shape. The top row corresponds to the experiment, while the bottom row shows the results of numerical finite element simulations, if available

tion **I**, except that one half of the near-boundary region is straight and the other half is curved causing twist and slight lift upward of the structure. Under weak perturbations the configuration **I*** switches to configuration **L**. It is worth to note that gravity influences the equilibria and when deactivated in numerical simulations, fewer stable configurations are obtained.

Two strain gauges SG_1 and SG_2 were embedded in the shell as shown in Fig. 1a, and the structure was then subjected to kinematic excitation at the clamp. The selection of two strain gauges, oriented along the x_1 axis, was made to provide the minimum number required for reliable indications in the static configurations. The strain gauge readings for the observed five equilibria are presented in Table 2. From a practical need, the strain gauges were calibrated for configuration **I**. The readings from strain gauges SG_1 and SG_2 can be classified into small values corresponding to significant curvature (in the transverse direction), and larger values corresponding to the shell's flattening at given regions.

Combining strain measures and numerical simulations validated in the static analysis, a proposal for a topographic map of potential energy V as a function of the relative elongation of strain gauges SG_1 and SG_2 is elaborated in Fig. 3. A set of five potential wells with ith local minima at strain gauges $(\overline{SG}_{1i}, \overline{SG}_{2i})$ and elliptic evolution with semi-major a and semi-minor b coefficients is proposed in the form

$$V(SG_1, SG_2) = V_{Ref} - \sum_{i=1}^{n=5}(V_{Ref} - V_i) \\ e^{\left(\frac{(SG_1-\overline{SG}_{1i})^2}{a_i}+\frac{(SG_2-\overline{SG}_{2i})^2}{b_i}\right)} \tag{2}$$

where V_{Ref} is the highest reference level of the strain energy, V_i denotes local extrema minima of the potential wells. It is noted that the area around a single potential well is equivalent to a linear stiffness (even for large deformations). However, the coexistence of at least two potential wells introduces strong nonlinearities into the system, which result from the proposed representative description based on Eq. (2), rather than from geometric nonlinearties in FE model constituted on the classical laminate theory. The proposed model also does not include the hysteresis occurring in the quasi-static jump between two configurations, discussed in depth for bistable composites, e.g. blooms [41,42]. Nevertheless, it is helps visualizing multiple wells of potential as well as the barriers required to overcome and achieve a different state of equilibrium.

3 Linear modal analysis

The pentastable structure was subjected to experimental modal tests using a contactless Polytec PSV-500 laser vibrometer system, compatible with Smart Shaker^{TM} K2007E01. A grid of 119 (7×17) measurement points was created on the shell's top surface. Small dynamic amplitude response in a wide frequency range of $0 - 100$ Hz were tested using an incremental frequency sweep. For small driving force the configuration **I*** loses stability. To maintain the highest quality, each marker was scanned three times. In the implemented algorithms, a set of time histories was subjected to a fast Fourier transform, resulting in collective amplitude-frequency curves presented in Fig. 4. For the first five resonant peaks in configurations **I**, **J**, **L**, **S** that correspond to a wide band natural frequencies, mode shapes are gathered in Fig. 5.

For very low frequency range up to 3.5 Hz, the composite structure has always the first bending modes about the x_2 axis. Moreover, for flattened the near-boundary region, regardless of the deformation of the second region (configurations **L** and **J**), the specimen exhibits exactly the same values of natural frequencies. For configurations **J**, **L** and **S** 2nd, 3rd and 4th vibration modes represent the 1st torsional mode, 2nd bending mode in the prone to bending direction and the 2nd twisting mode, respectively. In these setups, the second twisting modes frequencies are close, namely 31 ± 1 Hz. Configuration **I** exhibits both qualitatively and quantitatively different dynamic responses. The 2nd and 3rd mode shapes are coupled, indicating that their frequencies have nearly integer ratio $1 : 3$ while the nodal lines rotate. In contrast, the second twisting mode's frequency is significantly different from its analogous modes. Butterfly mode shapes for the 5th natural frequency are observed in configurations with curved second region (**I** and **L**), while the third bending modes are noted in configurations with flattened second region (**J** and **S**). Due to the specific curvature in configurations J and S, the third bending mode, despite minimal excitation in the transverse direction, may influence the system's response in the longitudinal direction. This can lead to strong nonlinear couplings through paramet-

Table 2 Strain gauge indications with respect to the observed stable configurations

Equilibrium	Strain gauge $\overline{SG}_1$ $\mu m/m$	Strain gauge $\overline{SG}_2$ $\mu m/m$
I-shape	0	0
J-Shape	5	795
L-Shape	790	165
S-shape	775	865
I*-shape	680	85
Free configuration	−64	−24

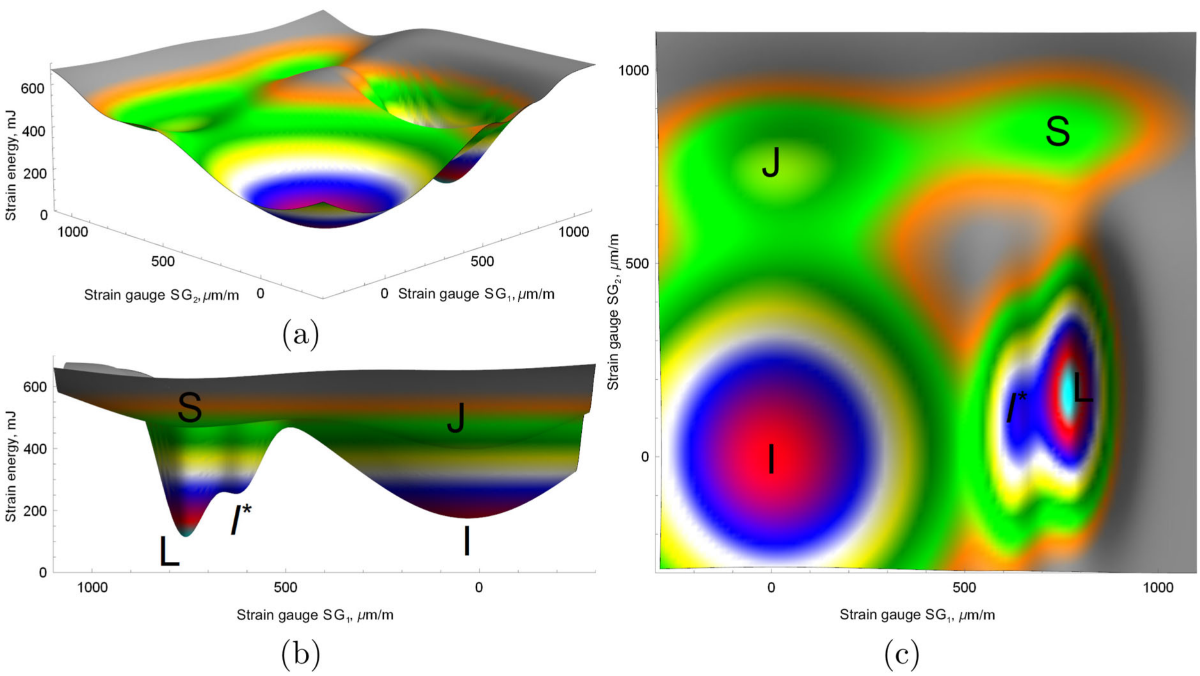

Fig. 3 Pictorial view of the pentastable system's strain energy topology: **a** isometric view from the top, **b** rear view and **c** top view

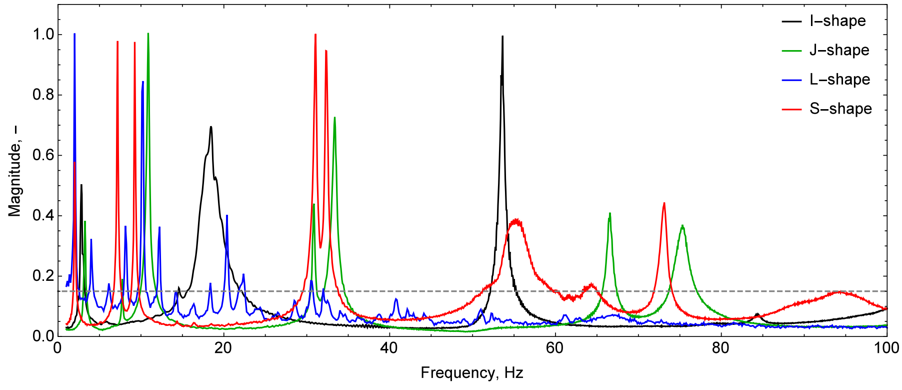

Fig. 4 Linear modal analysis pantastable shell

ric excitation, facilitating energy transfer to different vibration modes at higher oscillation amplitudes.

A satisfactory experimental and numerical model compliance of first five natural vibration modes and natural frequencies is achieved. Nevertheless, few, unavoidable, aspects affect the numerical model accuracy: (i) constant thickness is assumed across the entire surface in the free state, (ii) an ideal sequence of layers and linear material properties of the laminate are assumed, (iii) the boundary conditions in the clamp are idealized as a straight immovable in plane line, and (iv) vibration tests, despite using the contactless method, require mounting the exciter head near the clamp, which increases modal inertia in the system.

When multistability is exploited to conceive morphing structures, the configuration switching might be designed to broaden beneficial dynamic operating regimes. By considering the spectral properties shown in Fig. 4, several design indications can be inferred. Firstly, considering that the curves are scaled to 1 with respect to the highest peak of a given response, magnitudes above 15% marked by gray dashed line correspond to near-resonant regions. The resonant intervals in the measured range up to 100 Hz correspond to 43.97%; by limiting the frequency range to 40 Hz this resonant ratio increases to 58.35% and further frequency bandwidth reduction to 25 Hz the resonant coverage involving configurations **I**, **J**, **L**, **S** reaches 77.34%. This result is highly favourable for harvesting electrical energy from ambient mechanical vibrations. Additionally, a variety of resonant peak widths has been observed: most peaks are quite narrow, while those at 19 Hz for configuration **I**, 67 Hz and 77 Hz for configuration **J**, and 56 Hz and 73 Hz for configuration **S** are broader, indicating increased damping factors. For energy harvesting purposes, a convenient dynamic transition between configurations is achieved via first bending mode, because it involves the largest deformations. Such transition is triggered by the first shell region snap-through occurring for the configurations pairs **I-L** and **J-S**. Since all four natural frequencies are very close to each other, reversible jumps between different configurations is expected. Dynamic regimes of the different shell configurations associated to well separated resonance peaks are also worth to be considered. Finally, given the high modal density of configurations **J** and **S** in the 30–35 Hz frequency range, large amplitude oscillations for 1 : 1 internal resonances are expected. Moreover, further dynamic interactions like sub- super- harmonic and internal resonances are predicted.

4 Nonlinear oscillations

After having introduced the states of equilibrium and discussed their in-well modal analysis, we proceed to examine nonlinear dynamics regimes, characterized by moderate to large vibration amplitudes, where geometric nonlinearities play an important role [43].

4.1 Dynamic response to kinematic excitation

At the onset of the kinematic excitation, the shell was tested with amplitude of excitation $\xi = 1$ g across a vibration frequency range of $5 - 100$ Hz with a frequency sweep rate 0.18 Hz/s and utilized harmonic estimator. Time histories are also recorded during vibration tests and the following conversion was used to conveniently investigate the system's response in a frequency domain: $\Omega(t) = \Omega(t_0) + \alpha t$, where $\Omega(t)$ denotes the driving frequency, that starts at predefined startup frequency $\Omega(t_0)$ and varies in time t with a sweep rate α. The time of acceleration (5 s) and deceleration (5 s) process of the head expander is truncated from time signal. By substituting the range of forcing frequency and sweep rate, the test time can be easily calculated $t = 2\frac{\Omega(t_{max})-\Omega(t_0)}{\alpha} + 10$ s$\approx$ 1066 s$=$ 17 min 46 s. The frequency range including the lowest (1st) resonances of each stable configuration at this stage was excluded due to TIRA XXL electromechanical exciter hardware limitations. The scheme of the experimental setup is presented in Fig. 6 while the amplitude-frequency response curves for strain gauges SG_1 and SG_2 are shown in Fig. 7.

The dynamic response of configuration **I** presented in Fig. 7a, b shows two close peaks, corresponding to the third mode of vibrations coupled with the second one (see Fig. 5). The chosen distribution of the strain gauges makes it challenging to accurately measure torsional vibrations and bending in the stiffer direction (x_2). Note that the excitation, being applied along the whole clamped side of the shell, is quite ineffective for the torsional modes. Nevertheless, detected coupling in the modal analysis allows for the energy transfer and enhances the bending indications observed in this case. Unlike the laser vibrometry measuring the entire shell,

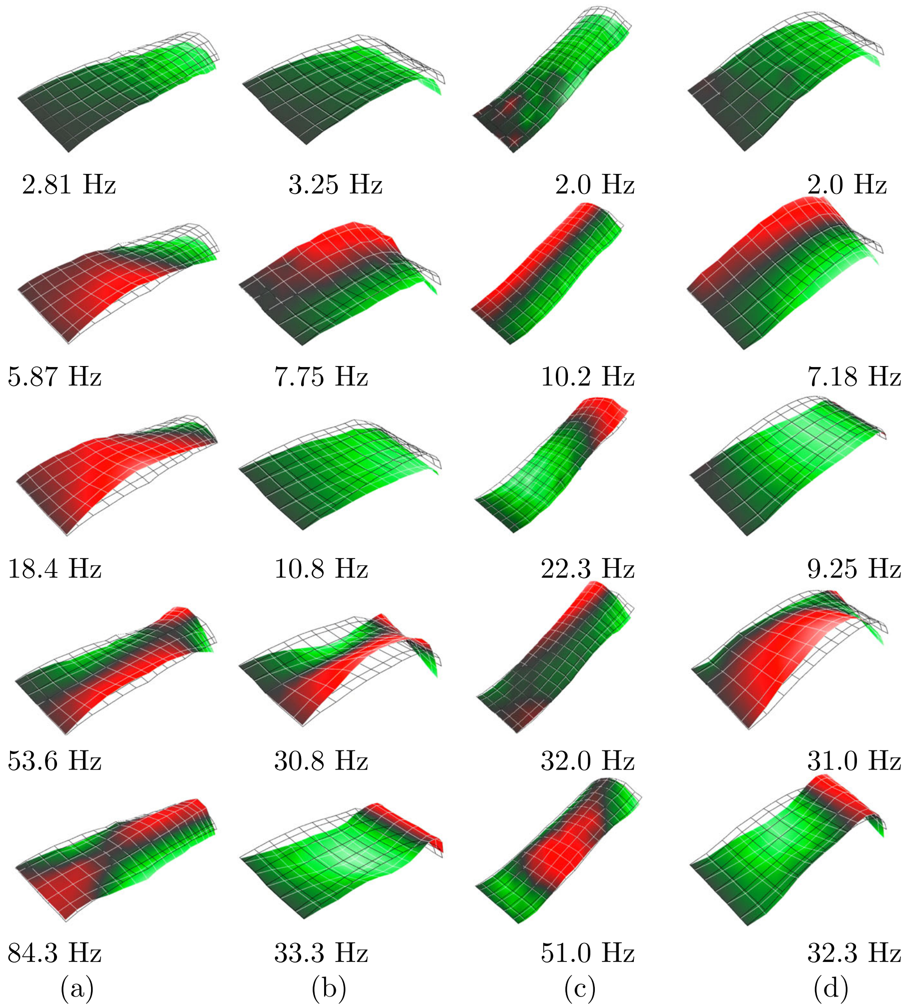

Fig. 5 The first 5 mode shapes with reported experimental natural frequencies for equilibria: **a** I-shape **b** J-shape, **c** L-shape and **d** S-shape

SG_1 and SG_2 sensors do not show increased values for the 4th and 5th modes of vibration.

In configuration **J**, the 2nd (3rd global) and 3rd (5th global) bending modes on the resonance curve from strain gauge SG_1 are shown in Fig. 7c. Figure 7d indicates the higher order bending mode with additional peak at 75 Hz for sensor SG_2. The strain gauge SG_1 does not detect this dynamic state due to close vicinity of the mode shape nodal line.

In configuration **L** the first twisting mode is captured by both sensors, as shown in Fig. 7e, f. This is once again caused by the coupling of torsional vibration with the second bending mode. The frequency response curve from 15 to 25 Hz strongly suggests internal resonance phenomenon. It involves the second bending mode with a natural vibration frequency of 22.3 Hz, which is coupled to the first torsional mode with a natural vibration frequency of 10.2 Hz through modal interactions (see Fig. 5). Moreover, given that the second torsion mode has natural frequency at 30.2 Hz, a special case of 1 : 2 : 3 internal resonance might be considered. This extremely interesting aspect will be investigated in following sections for higher amplitudes of excitation. A small resonance peak also occurs for the second twisting mode at 32 Hz. The last two peaks at 68 Hz and 78 Hz also indicate higher bending modes of the shell.

In the tested configuration **S** presented in Fig. 7g, h, the response of the second bending mode is dominant. The double peak at 32 Hz corresponding to the second twisting mode of vibrations and the third bending mode are separated by less than 3 Hz, but a small vibration response does not show coupling. The resonance at 55 Hz presents synchronisation between the

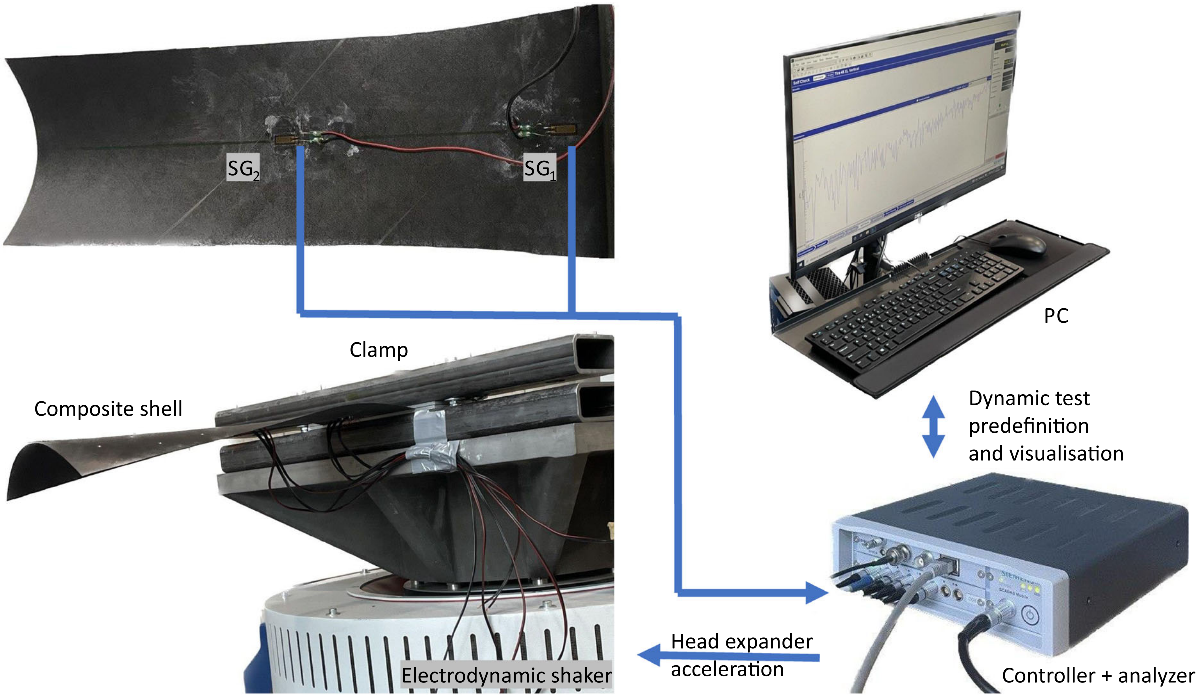

Fig. 6 Testing rig with instrumentation

first region having twisting behaviour (unmeasurable at sensor SG_1) and shell's second region showing locally the second flexural mode. Despite the structure being subjected to kinematic excitation in a direction susceptible to bending, for frequency range of $60-68$ Hz, the system's response occurs in the bending about a higher stiffness direction. It indicates that the shell induces motion in x_1x_2 plane via the nonlinear terms. Consequently, the strain gauge readings show a peak at twice the frequency of the second twisting and the third bending modes coupling.

In the following tests, the nonlinear dynamics in the vicinity of resonance peaks with a sweep rate $0.01 < \alpha < 0.1$ Hz/s, depending of frequency range, is examined. The considered experimental tests are carried out irrespective of the peaks' magnitude indicated by strain gauges in previous linear tests because their indications are not sufficient to evaluate the response of a given nonlinear vibration mode e.g. when strain gauges are located very close to a mode shape nodal line. The structure can oscillate in-well (locally within potential well), undergoing hardening or softening phenomena and potentially activating modal coupling. The main objective in forthcoming sections is to investigate dynamic regimes that enable transitions between distinct configurations, representing cross-well motion triggered by the snap-through effect. Furthermore, the snap-through phenomenon can be either one-way, where the structure remains in a new potential well, or reversible by snapping between two configurations. Specifically, reversible cross-well motion can be periodic, quasi-periodic, or chaotic. All these scenarios can be extended from cross-well dynamics between two configurations to a global dynamics, such as accounting for jumps between three or more potential wells.

I-Shape

The configuration **I** for the second bending mode has strong softening nature with asymmetric time history on strain gauge SG_2. For frequency sweeping forward and backward with amplitude of excitation $\xi = 1$ g, a jump between small and large vibration amplitudes with a tiny hysteresis range are shown in Fig. 8a, b. The resonance peak at 14.2 Hz corresponds to subharmonic resonance $1:4$ of the first twisting mode, due to its close proximity, coupled with the second bending motion showing almost equal magnitudes on

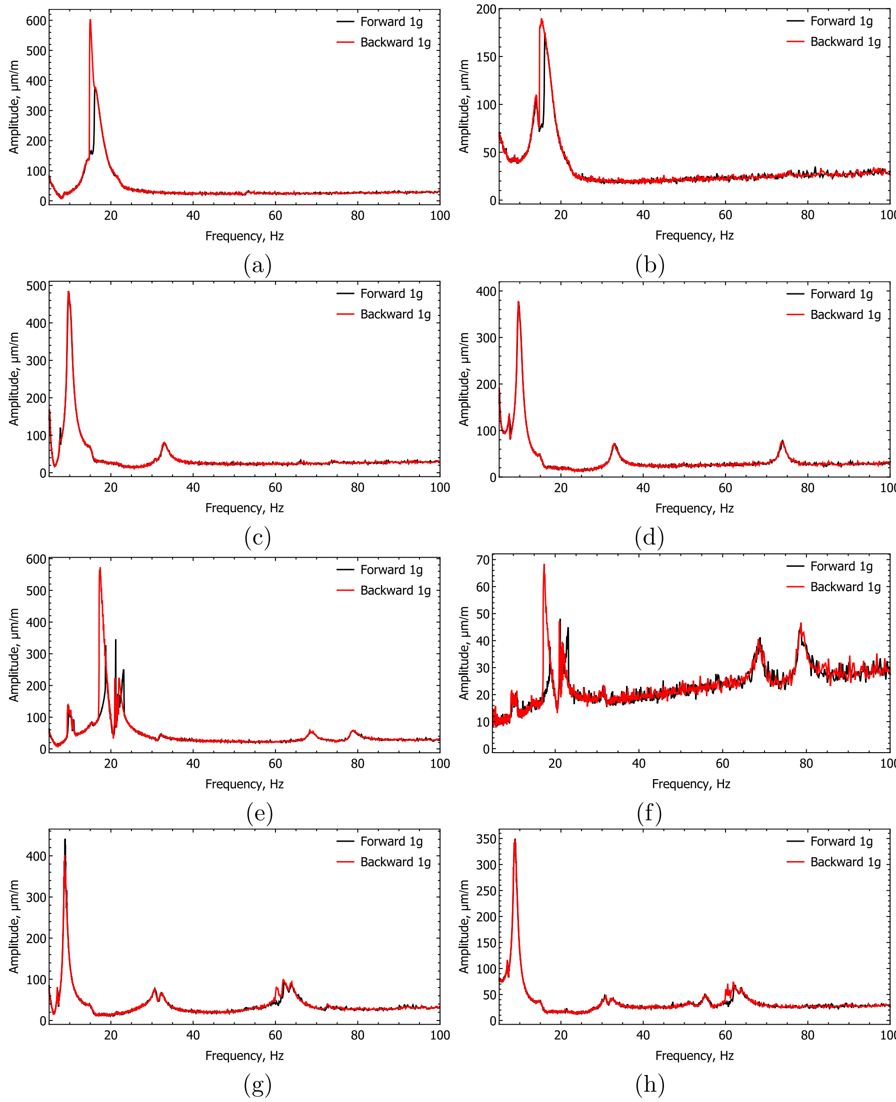

Fig. 7 Frequency response curves for amplitude of excitation $\xi = 1$ g, frequency sweeps forward and backward: **a, b** I-shape, **c, d** J-shape, **e, f** L-shape and **g, h** S-shape. Left (right) column corresponds to the strain gauge SG_1 (SG_2)

strain gauge SG_2. Small indications on the amplitude-frequency curve in Fig. 7 result from the estimator, which shows filtered responses with driving frequency and ignoring the other harmonics. Increasing amplitude of excitation to $\xi = 2$ g we can observe that the softening phenomenon has larger hysteresis, whereas the aforementioned coupled motion significantly increases its range towards lower frequencies in Fig. 8c, d. This behaviour is activated by the amplitude of deformation rather than frequencies coexistence, as evidenced by the exponential increase observed in the records from strain gauge $SG_1 \approx 100\ \mu$m/m.

Increasing the amplitude of excitation up to $\xi = 4$ g, two scenarios of escape from configuration **I** are presented in Fig. 8e, f. Starting with configuration **I** (red and blue curves), the coupled motion (involving first twisting and first bending modes) expands again towards lower frequencies. Due to the larger amount of energy pumped into the system, a jump to the configuration **L** is observed for the frequency sweep forward at 12 Hz. Next, the time history shows in-well oscillations up to 15.2 Hz. The system transits through a large amplitude twisting mode to cross-well dynamics between configurations **L** and **I*** up to 18.5 Hz, where it remains on the solution path corresponding to the left branch of the internal resonance and moves to the right branch of the internal resonance (see Fig. 7e). A further increase in frequency of excitation causes

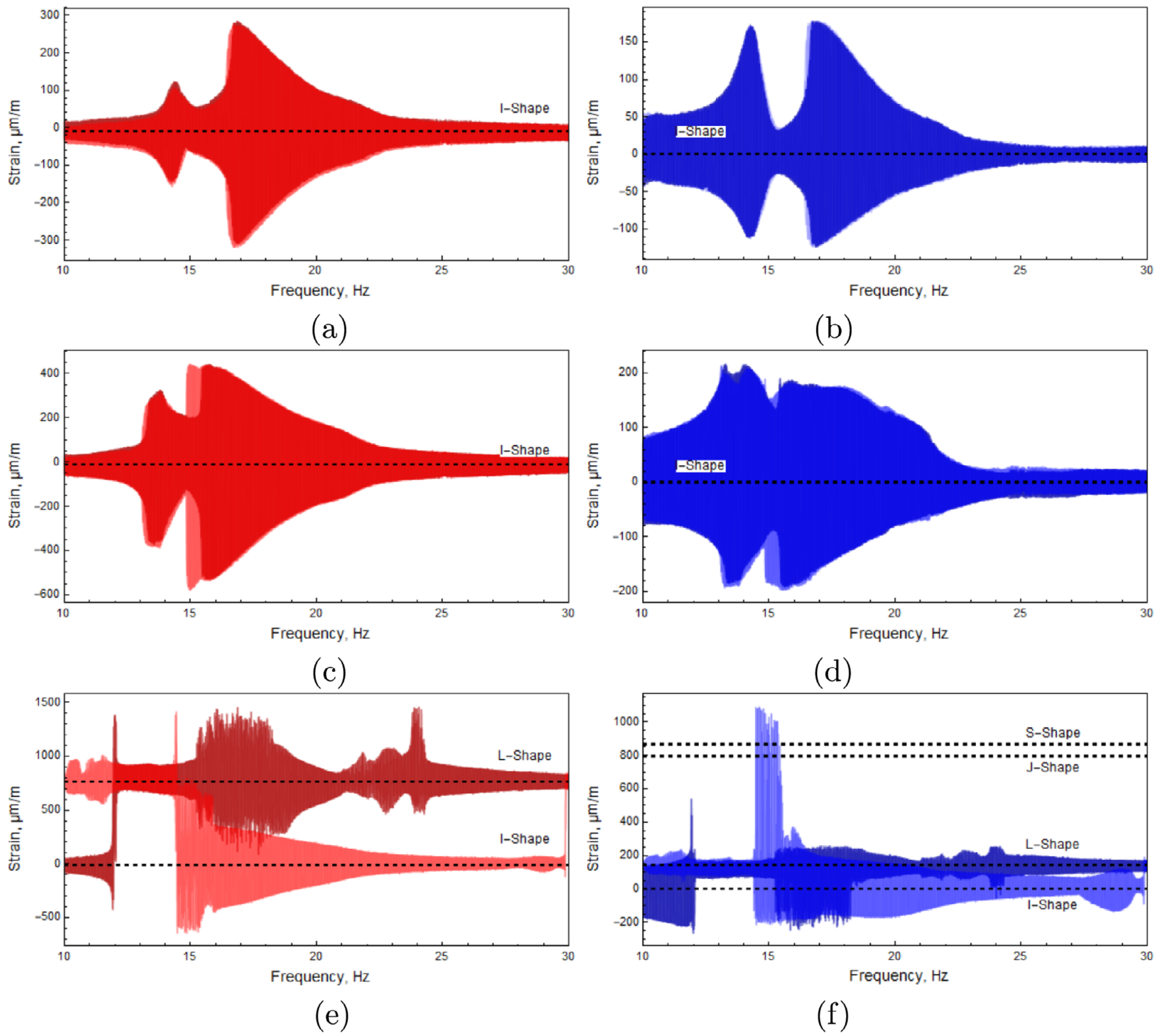

Fig. 8 Time series of the shell strain in initial I-shape equilibrium in the vicinity of the second bending mode for kinematic excitation: **a, b** $\xi = 1$ g, **c, d** $\xi = 2$ g and **e, f** $\xi = 4$ g (**a**). Left (right) column corresponds to the strain gauge SG_1 (SG_2), while red and blue (light red and light blue) colors denote frequency sweep forward (backward)

another range of jumps around the frequency of 24 Hz, and again this is a reversible snap-through effect between configurations $\mathbf{I}^*$ and **L** after which the indications remain around the equilibrium of configuration **L** up to 30 Hz. After completing the first test sequence, again the starting equilibrium is changed to configuration **I** and frequency sweep backward test begins (light red and light blue curves). Approaching the resonance of the second bending mode coupled with the twisting mode, we first observe global dynamics involving configurations **I**, $\mathbf{I}^*$ and **J**, starting at 15.5 Hz. At 14.5 Hz, the strain gauge SG_1 signal becomes sufficiently large that it indicates an escape to a new branch of the solution. The system remains in configuration **L**, returning neither to the predefined configuration **I** nor to the transitional ones ($\mathbf{I}^*$ and **J**).

From the results obtained so far, we conclude that the configuration $\mathbf{I}^*$ is oriented in between configurations **I** and **L**. Moreover it affects the system's dynamics, causes strongly nonlinear cross-well jumps which, under appropriate forcing parameters, evolve into global dynamics involving three equilibria: **I**, **I***, and **L**. Both scenarios of escape from configuration **I** involve interesting dynamic issues, the coupling of two modes or the global jump activation by cross-well motion. The two-way snap-through between configurations **I** and **L** does not occur because configuration **L** lacks resonating terms at given frequency band, and large velocities associated with the jump rapidly dissipate energy.

For configuration **I**, despite small indications on both strain gauges, the opportunity is taken to check the possibility of a jump around the fourth natural frequency at 53.6 Hz and fifth natural frequency at 84.3 Hz, corresponding to the second twisting and a butterfly modes, respectively (see linear mode shapes in Fig. 5). Cross-checking a higher frequency range allowed for a gradual increase in the excitation amplitudes up to $\xi = 20$ g. For the second twisting mode, a tilt toward left of the resonance peak with hysteresis effect represents the in-well softening effect in Fig. 9a, b. For excitation amplitude about $\xi = 16$ g, the twisting-bending coupling with integer ratio of nonlinear subharmonic frequencies $3 : 1$ is activated between 51 Hz and 53 Hz. In Fig. 9c, d, the butterfly mode also presents softening, however with a much smaller shift of resonance peak toward lower frequencies, without a double solution in the frequency domain. A snap to another configuration via both scenarios is not achieved.

J Shape

The dynamic responses for the first twisting mode (7.75 Hz) and the second bending mode (10.8 Hz) are shown in Fig. 10. For frequency sweep forward the first resonance peak shows that the twisting mode resonates at 8 Hz, then at 9.2 Hz the structure snaps-through and oscillates within configuration **S**, after which at 9.6 Hz the cross-well motion between configurations **J** and **S** is activated. As the frequency of excitation increases, the solution snaps-back to in-well motion of configuration **J**. The $1 : 2$ subharmonic resonance of the twisting motion is triggered at 14 Hz (see Fig. 10b) and expands up to 16 Hz after which it turns into the pure bending motion at 16.5 Hz. In the frequency sweep backward test, the $1 : 2$ subharmonic resonance of the twisting motion in the range of $14 - 15$ Hz is activated as well. Approaching the resonant frequency of the second bending vibrations mode, with negligible twisting, the solution path snaps to the configuration **S** in the close vicinity to a resonance of the given frequency. The further response remains in a new potential well showing the resonance of the second bending mode (9 Hz) and the first twisting mode (7 Hz), respectively. Here the mechanism of double-sided jump between two configurations is well exposed - the resonance curves of both configurations overlap. In the frequency range of 12-17 Hz by increasing amplitude of excitation up to $\xi = 5$ g an escape scenario from configuration **J** has not been observed.

The dynamic response in the frequency range of the second twisting (30.8 Hz) mode and the third bending (33.3 Hz) mode are shown in Fig. 11. Despite the closeness of the twisting and bending modes, the kinematic excitation does not activate the former one for either small or large vibration amplitudes. The in-well response of the second mode represent strong softening behaviour in Fig. 11a, b. For frequency sweep forward with amplitude of excitation $\xi = 9$ g shown in Fig. 11c, d, the response escape to configuration **S** at 29.3 Hz and resonates involving its second twisting and third bending modes up to 30.9 Hz where snaps-back to configuration **J**. Bypassing the configuration's **J** resonance range causes it to remain in its potential well until the forward test is completed. For the frequency sweep backward, the strain gauge SG_1 reading snaps to oscillations about 775 μm/m, where again second twisting and third bending modes of configuration **S** are activated until the end of the tested frequency range.

The 6th and 7th natural frequencies correspond to the third twisting (66 Hz) and fourth bending (74 Hz) modes, respectively. This frequency range is selected to explore potential for altering the configuration **J**, and the results are presented in Fig. 12. Similarly to the $1 : 2$ subharmonic resonance of the first twisting mode, for excitation above $\xi = 2$ g, activation of the coupled motion is observed on the strain gauge SG_2 when passing through a given frequency in Fig. 12b. Such a dynamic response does not indicate nonlinear characteristics, neither softening nor hardening. The fourth bending mode exhibits a softening nature. Increasing the vibration amplitude initially causes coupling with the third bending mode as $1 : 2$ subharmonic resonance (to the right of the resonance peak). Once this coupling is deactivated, higher amplitude records are observed on strain gauge SG_2. In the tested range, attempts to jump to other configurations have failed.

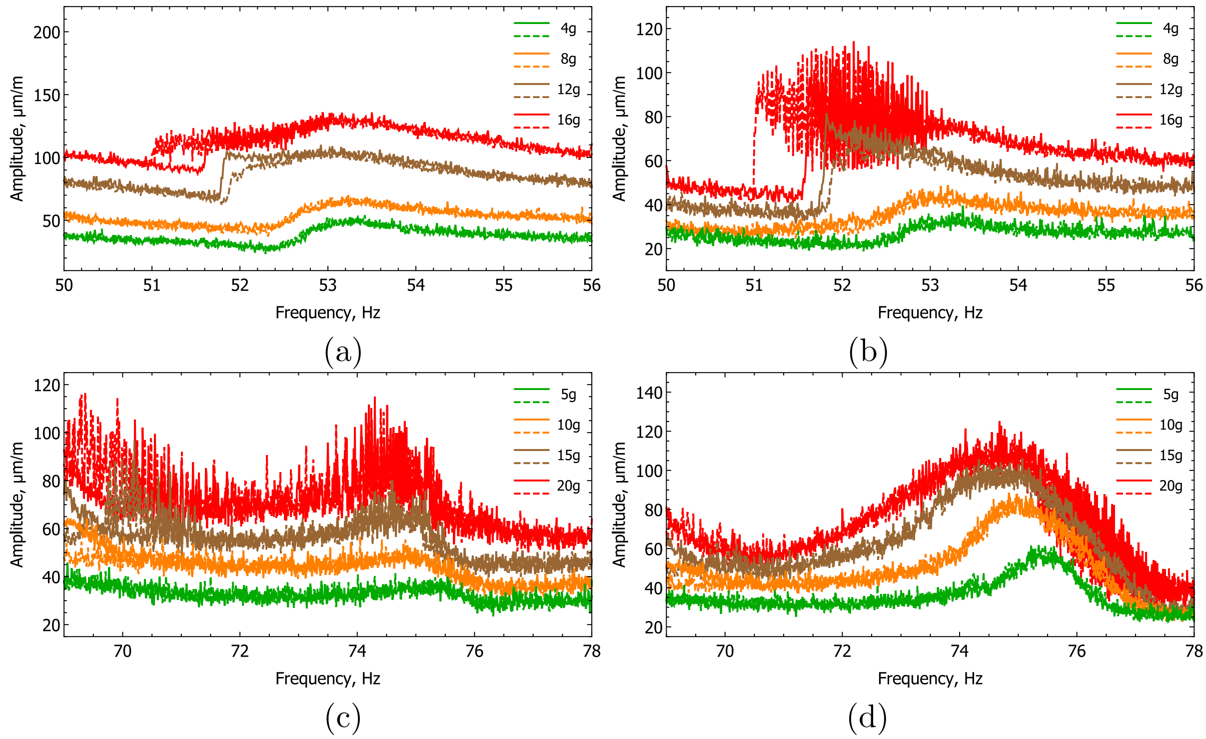

Fig. 9 Frequency response curves for sweep forward (solid line) and backward (dashed line) of configuration **I**: **a, b** fourth mode and **c, d** fifth mode. Left (right) column corresponds to the strain gauge SG_1 (SG_2)

L Shape

For configuration **L**, the dynamic response in the vicinity of the first twisting mode (10.2 Hz) shows a strong nonlinear interaction with the second flexural mode (22.3 Hz). The case of 1 : 2 internal resonance is presented in Fig. 13a, b and its counterpart case of 2 : 1 internal resonance is shown in Fig. 13c, d. In both cases, the left peak is responsible for the torsional mode, while the right peak represents the bending mode. For the first of two cases, increasing excitation amplitudes ($\xi = 2$ g, $\xi = 3$ g and $\xi = 4$ g), an area of unstable path is observed (from 10.8 Hz up to 11.2 Hz for $\xi = 4$ g). This instability is well known in literature and represents the source-type solution branch [44]. The dynamics of internal resonance facilitate the amplification of system deformation amplitudes, leading to a transition between configurations **L** and **I*** for amplitude of excitation $\xi = 4$ g within the frequency range of 8.9−9.4 Hz for frequency sweep in both directions. It is noticed that the right tongue of resonance curve reaches higher values but still do not activate the global motion, therefore, the twist of shell's near-boundary region is crucial here.

In the case of 2 : 1 internal resonance, gradually increasing the amplitude of excitation to $\xi = 4$ g and $\xi = 5$ g, the system's response achieves higher values. As a result, the two-way snap-through effect between configurations **L** and **I*** occurs at both peaks, as shown in Fig. 13e–h. Considering the left peak separately, it can be observed that for both amplitudes of excitation $\xi = 4$ g and $\xi = 5$ g, the required condition to activate the jump is about 800 μm/m on strain gauge SG_1 and 120 μm/m on strain gauge SG_2. Upon reaching these values, the system transitions to the new cross-well branch of its response. On the right hand side peak for the frequency sweep forward, this mechanism does not apply because the twisting overlaps bending, which activates the configuration **I***. Nevertheless, two different branches of the solution are detected: one where twisting is activated and snap-through occurs (higher values), and another with the mono-modal bending response (lower values). Due to the fact that the shell in configuration **L** has the lowest

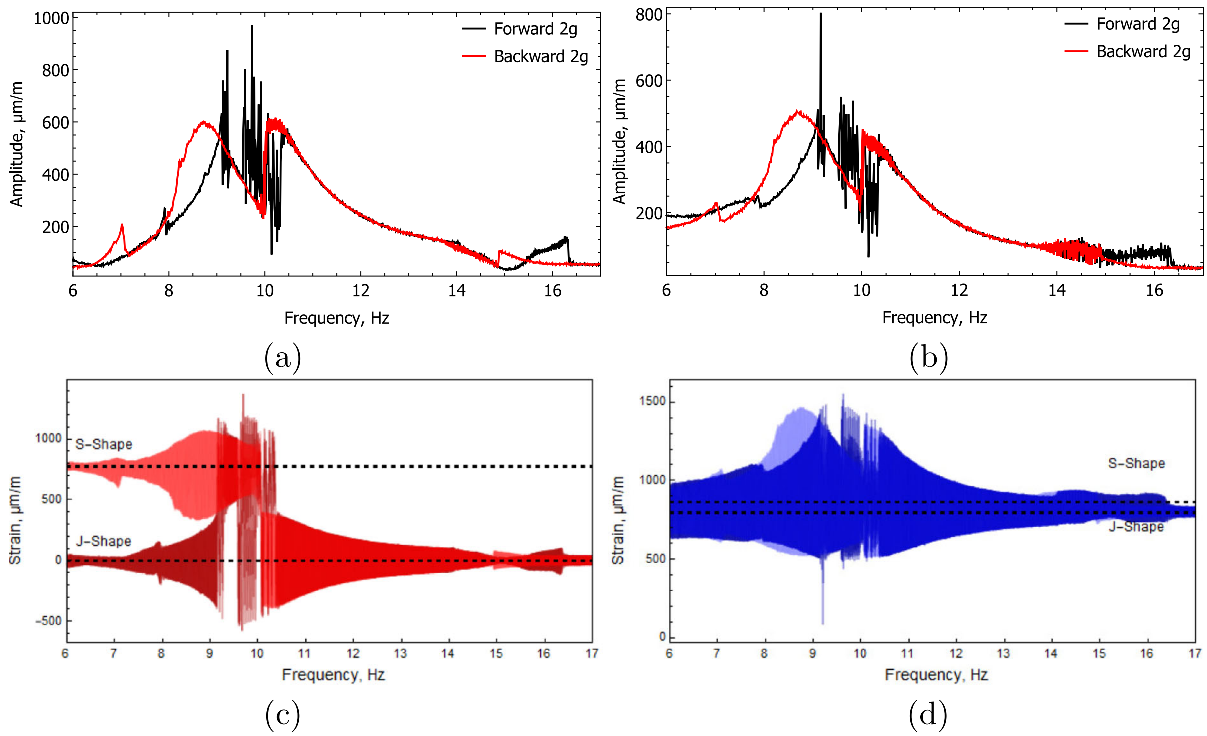

Fig. 10 Frequency response curves (**a, b**) and time series (**c, d**) of the shell strain in initial configuration **J** with the transition to configuration **S** through the second bending mode. Left (right) column corresponds to the strain gauge SG_1 (SG_2)

level of potential energy and the configuration **I*** has an extremely shallow potential well, there is no sufficient barrier to remain in the latter configuration. Consequently, despite dynamic couplings, the deformation field always returns to the pre-set configuration. It is expected that increasing the forcing amplitude would allow to jump to the configuration **I** and to remain there within the non resonant ranges of approximately 10-12 Hz and 16-20 Hz, or to undergo a continuous global snap-through in the range of 12-16 Hz when both configurations resonate.

For kinematic excitation presented in Fig. 7e, f, the third resonance peak represents the second twisting mode. The examination of given frequency range for larger excitation amplitudes is shown in Fig. 14. Bearing in mind that the harmonic estimator is used to generate the resonance curves, we conclude that for excitation amplitude $\xi = 3$ g two ranges with two solution branches are detected. On strain gauge SG_1 in the range of $30 - 30.5$ Hz the first bifurcation is observed, and the second one involves both strain gauges (SG_1 and SG_2) in the frequency range of 31.8-33 Hz. In both cases of larger indications, the additional mode is activated. A low level of noise in the postprocessed signal indicates the system's response with a pure second torsional mode of vibration. As the system passes through resonance, which increases deformation and activates couplings with the first torsional mode ($10.2 \times 3 = 30.6$ Hz), the noise level increases significantly due to $1:3$ subharmonic resonance. Increasing the excitation amplitude to $\xi = 6$ g extends the hysteresis range to higher frequencies, while the left area goes almost beyond the tested range. Successive enlarging amplitudes of excitation up to $\xi = 9$ g and $\xi = 12$ g only one bifurcation is observed within the tested frequency range. Despite the significant vibration amplitudes and strain gauges indications above $SG_1 = 500$ μm/m and $SG_2 = 200$ μm/m, and the combined response of twisting modes, a jump to the configuration **I*** have not been detected.

The last two resonance peaks of configuration **L** corresponds to butterfly (left) and bending-twisting (right) modes. Due to the frequent occurrence of internal resonances and not very distant frequencies, they were

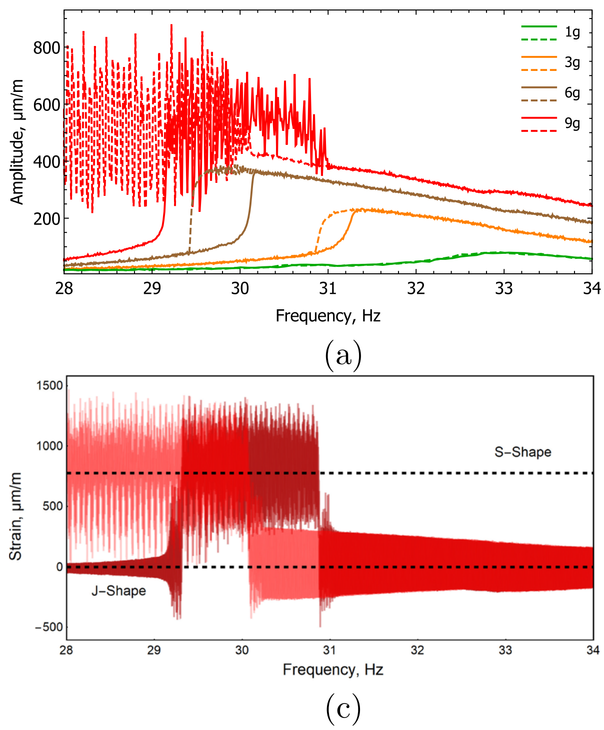

Fig. 11 Frequency response curves (**a, b**) and time series (**c, d**) of the shell strain in initial configuration **J** and transmission to the configuration **S** through the third bending mode. Left (right) column corresponds to the strain gauge SG_1 (SG_2), while red and blue (light red and light blue) colors denote frequency sweep forward (backward)

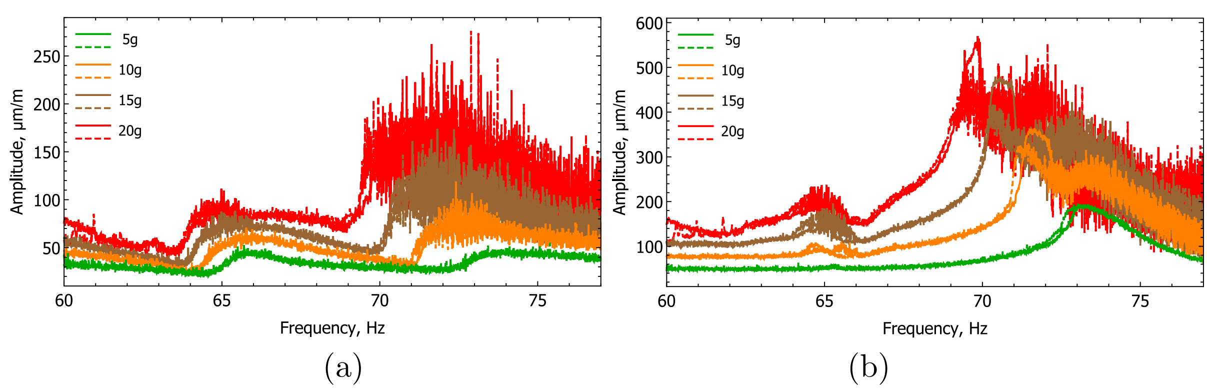

Fig. 12 Frequency response curves of the shell in configuration **J** for higher order resonances. Left (right) column corresponds to the strain gauge SG_1 (SG_2)

tested in a single experiment, and the results are presented in Fig. 15. Both resonance areas show a significant tilt of the frequency response curves toward left, indicating a softening nature. The large excitation amplitude of $\xi = 20$ g causes both areas to merge, and the interaction between them as a $1 : 1$ resonance leads to a quasi-periodic response.

S Shape

Large amplitude response of the configuration **S** for frequency bandwidth near the first twisting (7.18 Hz) and second bending (9.25 Hz) modes are shown in Fig. 16. Activation of the twisting mode for amplitude of excitation $\xi = 1$ g generates a drift of the system

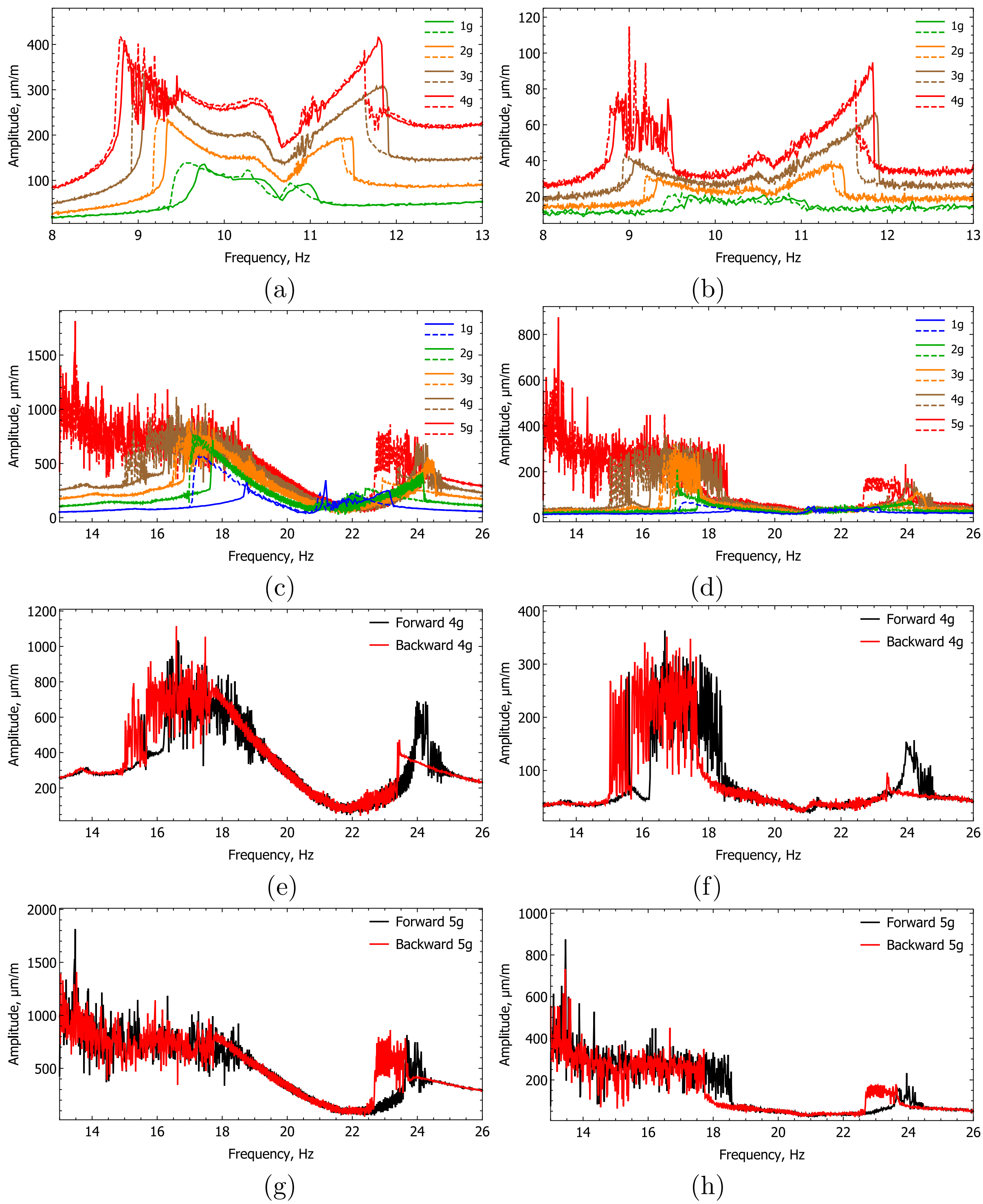

Fig. 13 Frequency response curves for internal resonances between twisting and bending modes of configuration **L**: (**a**–**d**) frequency sweep forward (solid lines) and backward (dashed lines). Separated curves for larger amplitudes of excitation: **e, f** $\xi = 4$ g, and **g, h** $\xi = 5$ g. Left (right) column corresponds to the strain gauge SG_1 (SG_2)

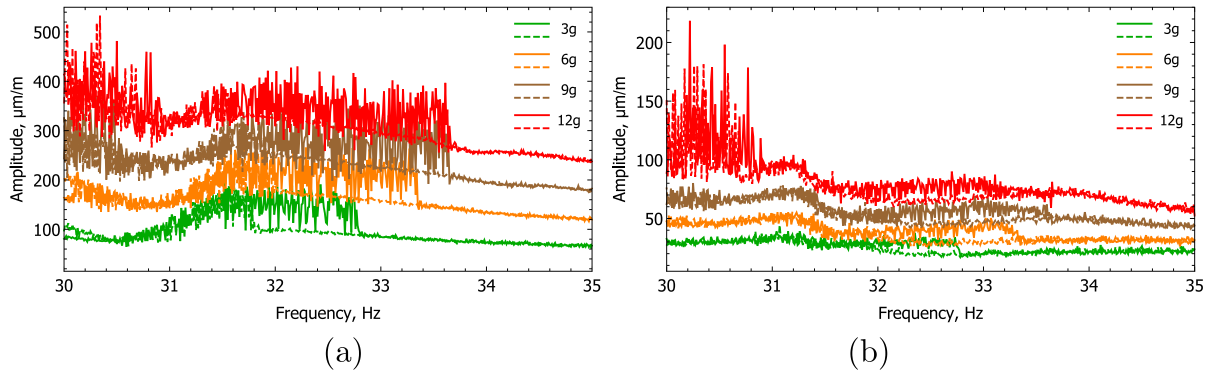

Fig. 14 Frequency response curves of configuration **L**: the case of 1 : 3 subharmonic resonance between the second twisting and the first twisting modes. Left (right) column corresponds to the strain gauge SG_1 (SG_2)

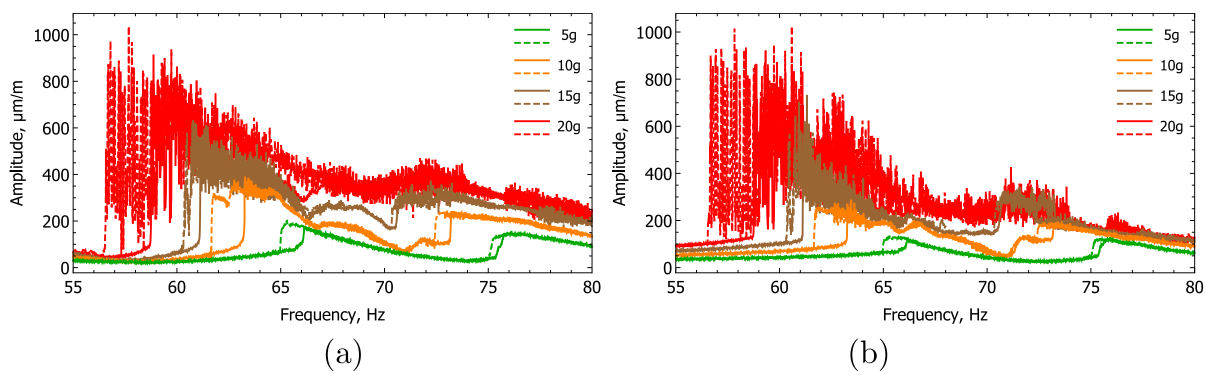

Fig. 15 Frequency response curves of configuration **L**: the case of 1 : 1 resonance between higher order modes. Left (right) column corresponds to the strain gauge SG_1 (SG_2)

response, causing hysteresis of the solution in a small range 7-7.3 Hz. By increasing the amplitude of excitation, the double solution area gradually widens for $\xi = 2$ g, $\xi = 3$ g and $\xi = 4$ g, for the highest two values leading to a jump to the configuration **J**. A similar phenomenon has already been observed in Figs. 10 and 13, however, in the present case it turns out to be very useful in escaping configurations **J** and **S** for frequency sweep forward shown in Fig. 16c, e, and frequency sweep backward reported in Fig. 16e. The second bending mode for amplitudes of excitation $\xi = 1$ g and $\xi = 2$ g exhibits a slight softening nature and do not reach the transition between configurations. For frequency sweep backward, in a narrow range between 8.5 and 9 Hz for the amplitude of excitation $\xi = 3$ g, and then between 7.8 Hz and 9.3 Hz for the $\xi = 4$ g, the cross-well oscillations with reversible snap-through effect are observed. Note that in Fig. 16c–d and Fig. 16e–f, the dynamic response for a forward frequency sweep with amplitudes of excitation $\xi = 3$ g and $\xi = 4$ g approaches the resonance zone via the second bending mode of configuration **J**. The critical deformations required to release cross-well motion are reached at increasingly lower frequencies. The low frequency range 8.25-10.6 Hz is the broadest range that has shown dynamic jumps in tests conducted so far.

In configuration **S**, natural frequencies of the second twisting (31 Hz) and the third bending (32.3 Hz) modes are close to each other. Dynamic responses to the kinematic excitation in the resonant region are shown in Fig. 17. For a small amplitude of oscillations both peaks are shifted toward left with respect to the modal analysis and the amplitude of excitation $\xi = 1$ g (see Fig. 7g and 7), it again suggests softening nonlinearities in both resonances. For the frequency sweep forward, the amplitude of excitation change to $\xi = 6$ g activates the 1 : 3 subharmonic resonance of the second bending mode (26.2-28 Hz), and then at 28.7 Hz bifurcates to

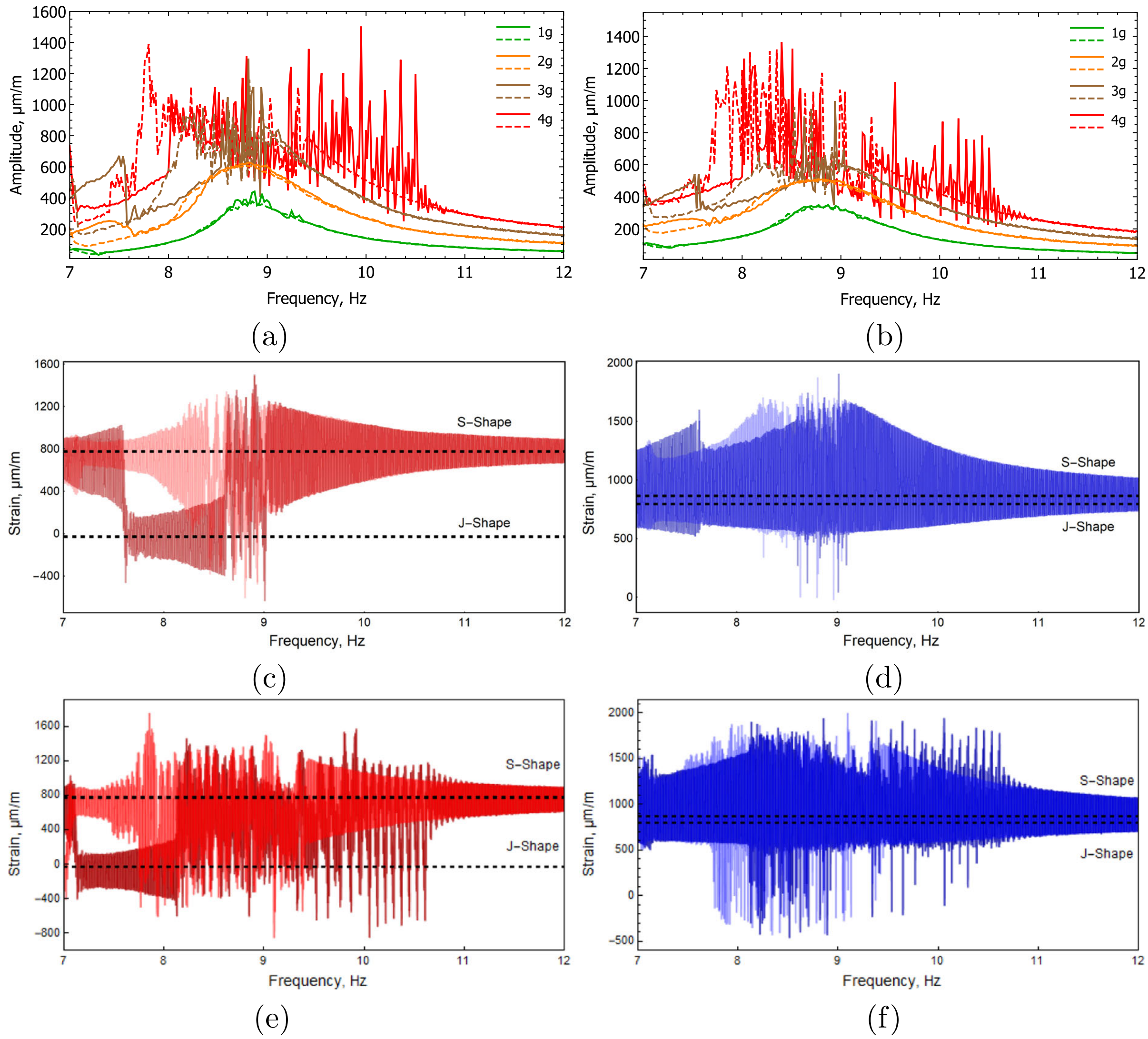

Fig. 16 Frequency response curves (**a, b**) and selected time series for $\xi = 3$ g (**c, d**), $\xi = 4$ g (**e, f**) of the shell strain in initial configuration **S** with transmission to the configuration **J** through the second bending mode. Left (right) column corresponds to the strain gauge SG_1 (SG_2)

cross-well oscillations between configuration **S** and a new dynamic configuration, very close to **J**, but according to Table 2, still not achieving the accepted in static regime the magnitude on the strain gauge SG_1.

4.2 Qualitative analysis of motion nature

To characterise the structure's in-well, cross-well and global dynamics, for each shell's stable configuration, a step tests at given frequency of excitation Ω with incremental amplitude of excitation ξ are performed. Experimental time courses are projected onto phase planes, and corresponding stroboscopic maps are generated from these projections. The dynamic regimes resulting from the response data will be classified into periodic, quasi-periodic, and chaotic behaviour candidates.

Figure 18 presents step test for initial configuration **I**. For small amplitudes of excitation 0.5 g$\leq \xi \leq 3.5$ g the in-well responses have ellipsoidal shape with one small loop at strain gauge SG_1 corresponding to sub-

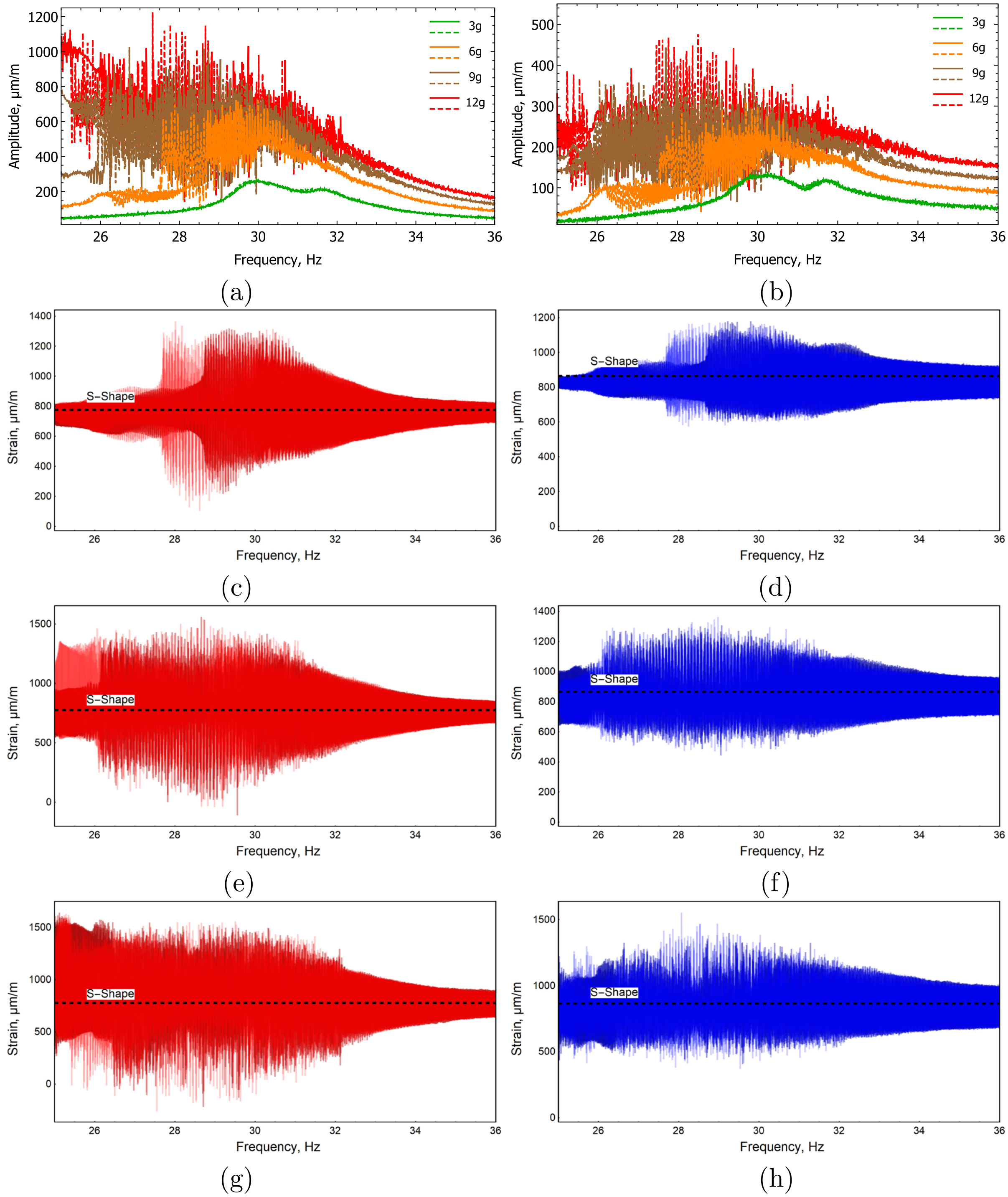

Fig. 17 Frequency response curves (**a, b**) and selected time series for $\xi = 6$ g (c, d), $\xi = 9$ g (**e, f**), $\xi = 12$ g (**g, h**) of the shell strain in initial configuration **S**: the case of 3 : 1 subharmonic resonance. Left (right) column corresponds to the strain gauge SG_1 (SG_2)

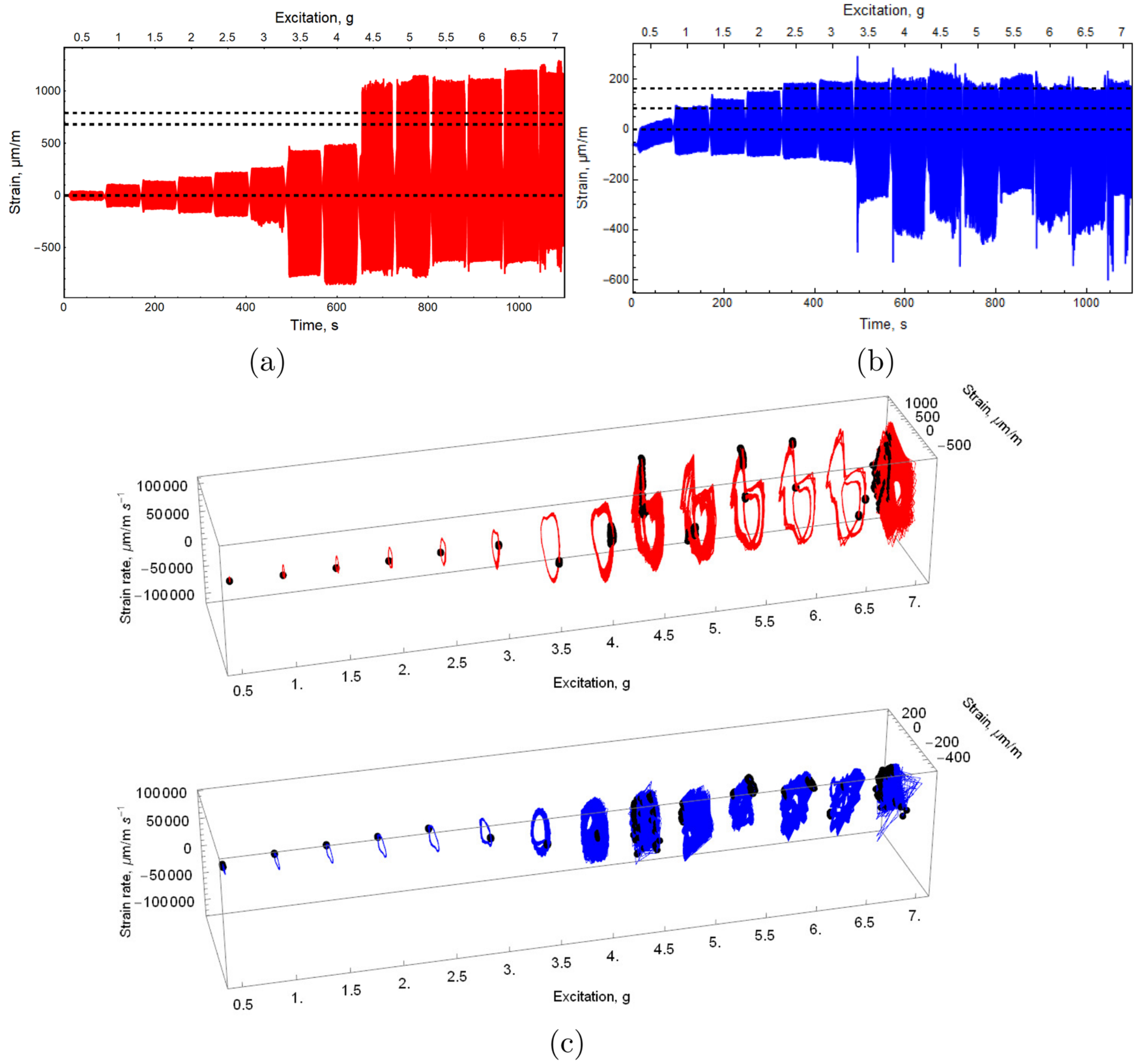

Fig. 18 Step test for initial configuration **I**, fixed frequency of excitation 15 Hz and gradually increased amplitude of excitation: time evolution of (**a**) strain gauge SG_1, (**b**) strain gauge SG_2 and (**c**) selected 825 cycles for phase portrait (line) with Poincaré map (black points)

harmonic bending-twisting interaction. Increasing the excitation amplitude to 4 g a quasi-periodic response with the stroboscopic points forming an ellipse is captured. Recalling Fig. 8, the left resonance and right resonance peaks merges. Further gradual steps of driving force ($\xi = 4$ g, $\xi = 4.5$ g and $\xi = 5$ g) result in a reversible snap-through between the potential wells **I** and **L**. Interestingly, just after crossing the barrier, at strain gauge SG_1 the stroboscopic points are divided into two subgroups: (i) associated with the original potential well (SG_2 <500 μm/m) represents a set of points gathered in one place and (ii) dispersed in the new potential well (SG_2 >500 μm/m), which suggests a quasi-periodic response or even a chaotic response. On the contrary, only $\xi = 4.5$ g for the strain gauge SG_2 indicates a random distribution of stroboscopic points, while planes for $\xi = 5$ g and $\xi = 5.5$ g suggest only quasi-periodic motion (the latter with period

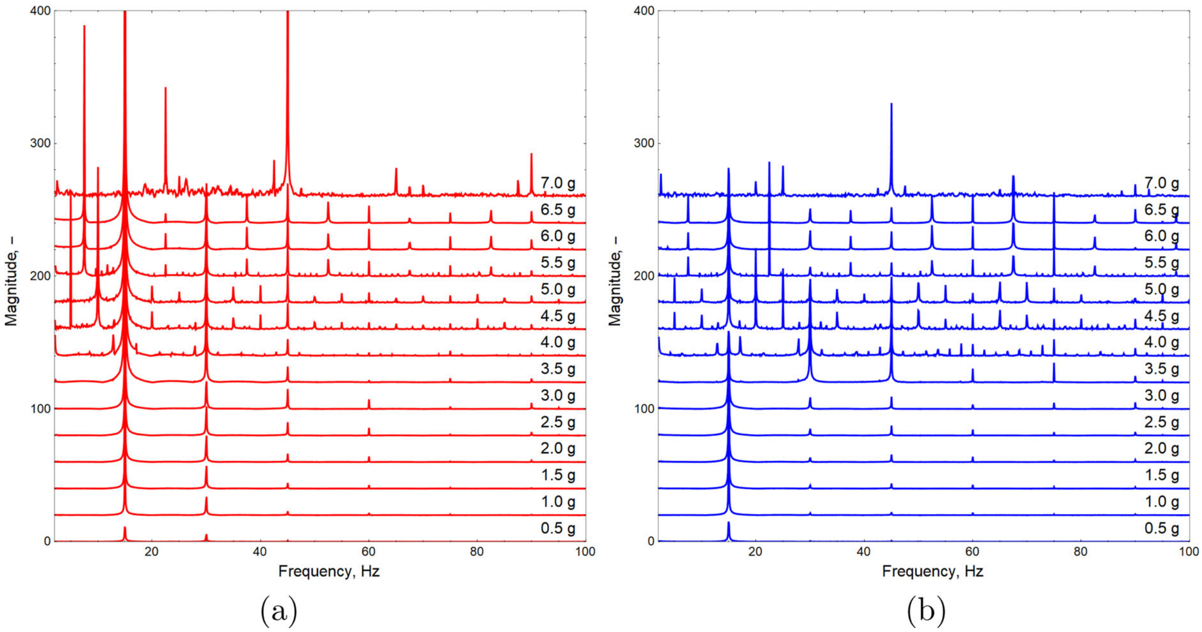

Fig. 19 Fast Fourier transform of step test (Fig. 18) for initial configuration **I**, fixed frequency of excitation 15 Hz and gradually increased amplitude of excitation: frequency spectra of (**a**) strain gauge SG_1 and (**b**) strain gauge SG_2. To increase the clarity of the results, the readings of each curve are raised successively by 20 units

doubling). It appears to be logical because the snap-through mechanism is in the first region and the sensor SG_1, while the indications on the strain gauge SG_2 mainly concern the second region, which is only indirectly affected by multiple harmonics that slightly disturb the dominant driving frequency Ω. Time histories for $\xi = 6$ g and $\xi = 6.5$ g have a regular but still strongly nonlinear nature with period doubling. Finally the system emerges to quasi periodic or chaotic response at $\xi = 7$ g. The structure returns to its original configuration **I** after each excitation interval.

For frequency analysis, the time histories of the step test are subjected to a fast Fourier transformation, as shown in Fig. 19. Stripes associated with frequency of excitation $\Omega = 15$ Hz appear at both strain gauges for all amplitudes of excitation. Only integer multiples of the driving frequency are also activated frequencies in the range of 0.5 g$\leq \xi \leq 3.5$ g. When the excitation amplitude increases to $\xi = 4$ g, finitely many evenly distributed peaks are observed. For $\xi \geq 4.5$ g, the cross-well motion presents even more activated frequencies suggesting the possibility of chaotic behavior for $\xi = 4.5$ g, $\xi = 5.5$ g, and $\xi = 7$ g. The curves $\xi = 5$ g, $\xi = 6$ g and $\xi = 6.5$ g do not have such effect and are classified as periodic motions.

Both stroboscopic maps and fast Fourier transforms indicate chaotic response candidates. To further confirm this, maximum Lyapunov exponents are calculated from the experimental time series following the procedure described in [45]. Chaotic behavior is confirmed for $\Lambda_{max}(\xi = 4\text{ g}) = 0.0383$, $\Lambda_{max}(\xi = 4.5\text{ g}) = 0.0268$, $\Lambda_{max}(\xi = 5.5\text{ g}) = 0.0257$ and $\Lambda_{max}(\xi = 7\text{ g}) = 0.0717$, while the remaining exponents are negative or negligibly small.

A mechanism of one way switch from configuration **J** to configuration **S** is presented in Fig. 20. Apart from the largest considered vibration amplitude, for the pivotal strain gauge SG_1 Poincaré maps and phase planes in the steady state exhibit periodic motion with a single driving harmonic. The excitation amplitude of $\xi \leq 3$ g is sufficient to activate a unidirectional jump, accounting for the cross-well dynamics. It is noted that once the structure escapes configuration **J**, the snap-back must be manually imposed before subsequent tests. On the contrary, the in-well oscillations for strain gauge SG_2 are mainly quasi-periodic. Moreover, the excitation $\xi = 4$ g shows nonlinear activation

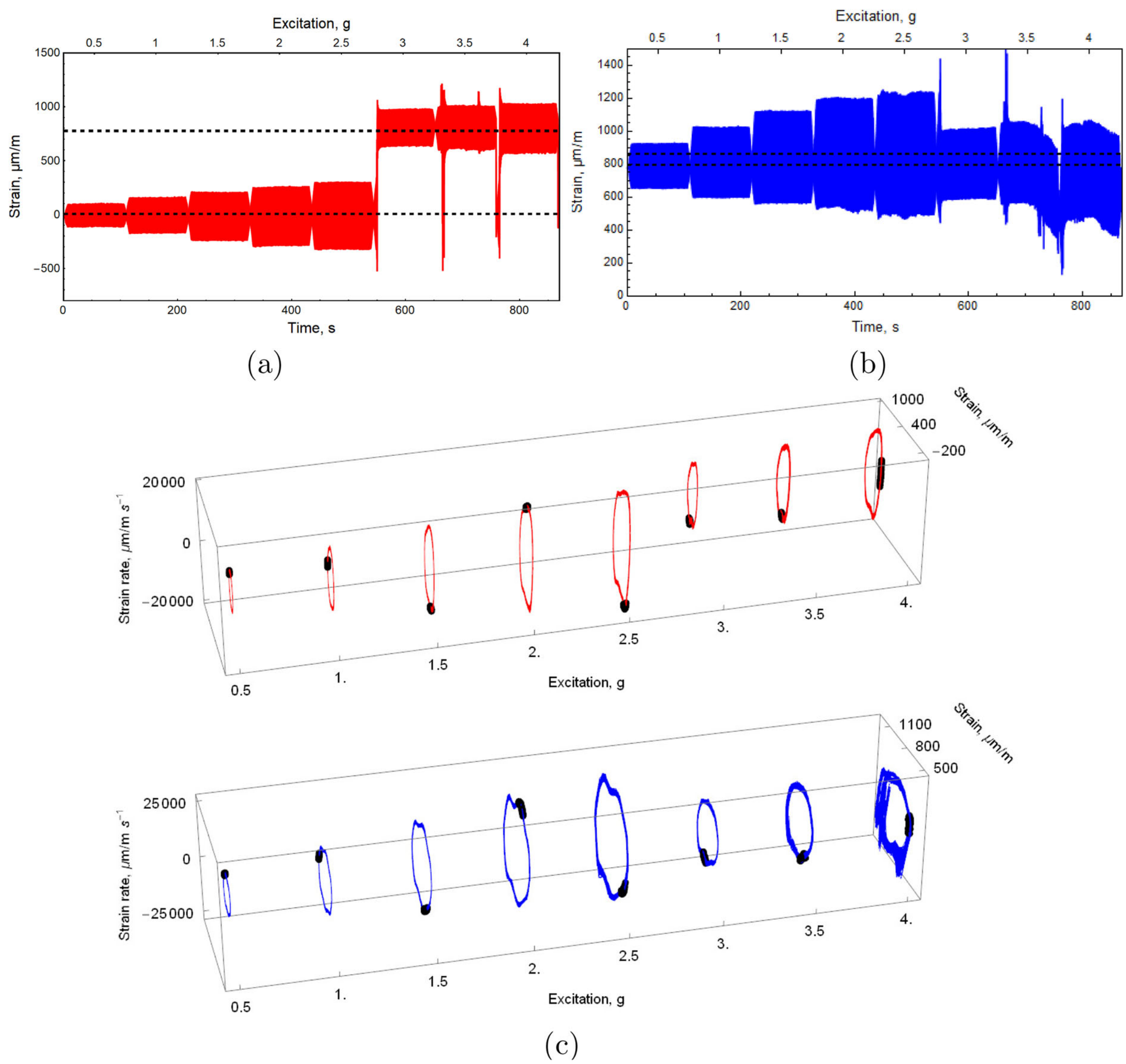

Fig. 20 Step test for initial configuration **J**, fixed frequency of excitation 10.5 Hz and gradually increased amplitude of excitation: time evolution of (**a**) strain gauge SG_1, (**b**) strain gauge SG_2 and (**c**) selected 262.5 cycles for phase portrait (line) with Poincaré map (black points)

of torsional motion by transforming phase planes from regular ellipsoidal to more involved one.

Responses evolution for configuration **L** at frequency $\Omega = 22.5$ Hz corresponding to 2:1 internal resonance of Fig. 13c–h for amplitudes of excitation from $\xi = 0.5$ g up to $\xi = 13$ g with a step 0.5 g are shown in Fig 21. Even from the smallest excitation amplitudes it shows quasi periodic in-well responses. For the continuous increase of the excitation, the envelope of the system response on the strain gauges SG_1 and SG_2 first increases up to 800 μm/m (peak to peak) for $\xi = 3$ g and then decreases to 350 μm/m (peak to peak) for $\xi = 8.5$ g, followed by a qualitative change in the response that has the symptoms of chaos behaviour - involving the global dynamics passing through the three potential wells of configurations **L**, **I** and **I***.

Figure 22 shows the step test at frequency of excitation $\Omega = 9$ Hz for reversible snap-through between

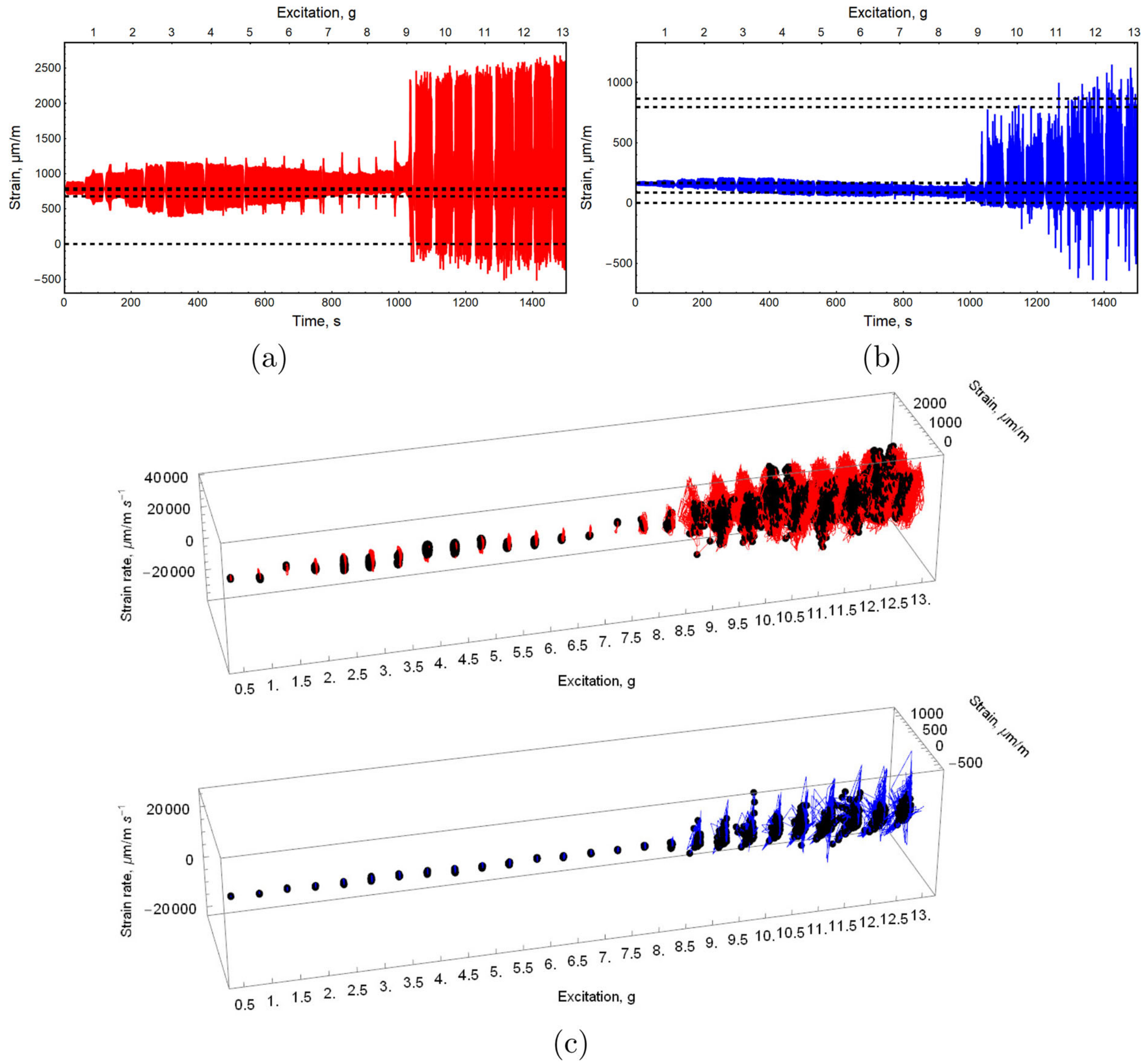

Fig. 21 Step test for initial configuration **L**, fixed frequency of excitation 22.5 Hz and gradually increased amplitude of excitation: time evolution of (**a**) strain gauge SG_1, (**b**) strain gauge SG_2 and (**c**) selected 562.5 cycles for phase portrait (line) with Poincaré map (black points)

configurations **S** and **J** corresponding to cross-well dynamics of Fig. 16. The kinematic excitation near second bending mode causes an asymmetric time histories of strain gauge SG_1 and symmetric response on strain gauge SG_2 for in-well motion. Amplitude of excitation below $\xi < 3$g presents mono-harmonic in-well dynamics. Once the magnitude of excitation is $\xi = 3$ g the indication on strain gauge SG_2 exceed negative values, which may incorrectly suggest that the potential well of configuration **J** has been reached. However, the phase plane projection and the corresponding stroboscopic maps show no signs of snap-through. Despite achieving an appropriate level of strain gauge readings, the jump mechanism at the interior-segment of the shell has not yet been achieved. A slightly greater amplitude of excitation ($\xi < 3.5$ g) activates the jump on strain gauge SG_2. Interestingly, such a large portion of energy is released that the grip part also shows jumps between

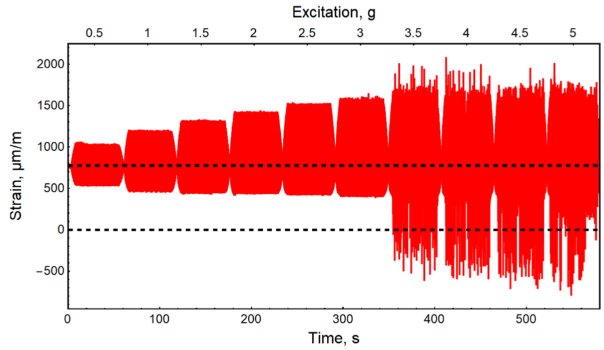

(a)

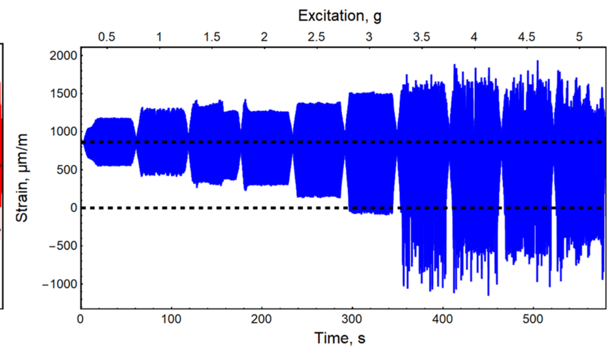

(b)

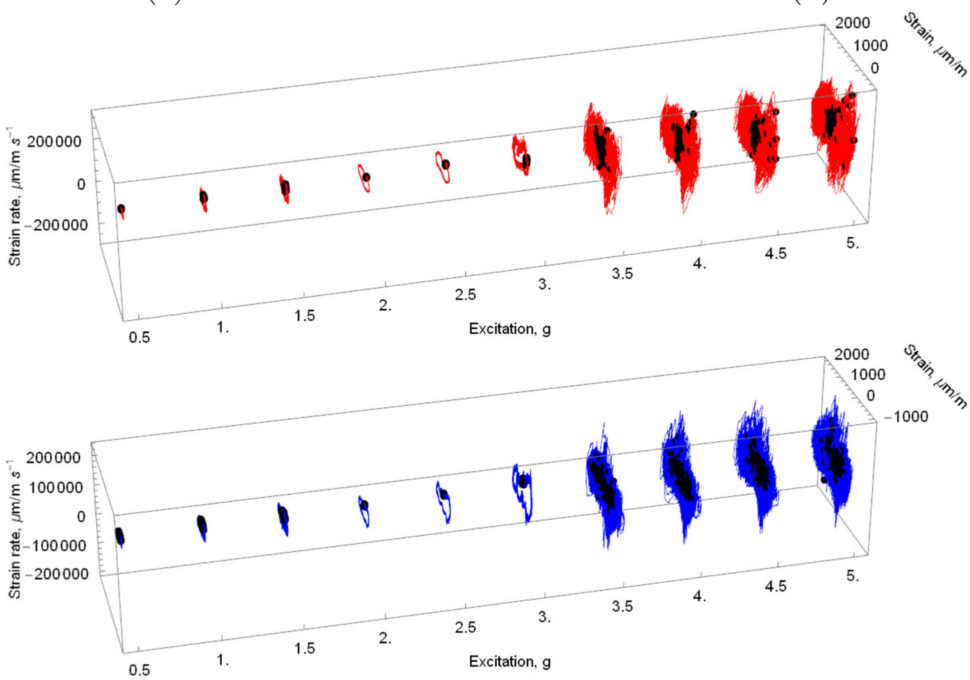

(c)

Fig. 22 Step test for initial configuration **S**, fixed frequency of excitation 9 Hz and gradually increased amplitude of excitation: time evolution of **a** strain gauge SG_1, **b** strain gauge SG_2 and **c** selected 180 cycles for phase portrait (line) with Poincaré map (black points)

the straight and original indication. This motion type is classified as global chaotic dynamics, possibly involving all five equilibria.

5 Conclusions and further developments

A composite conical shell featuring opposite curvatures (type B), was experimentally investigated after being one-sided clamped, revealing five stable equilibria: **I**, **J**, **L**, **S**, and **I***. In the static study, a comparison between numerical and experimental configurations was provided for four of the five stable states. Based on the calculated stored strain energy from the numerical model and the strains obtained from experiments, a visual representation of the pentastable system potential energy scenario was proposed.

In the linear modal analysis, a wide frequency range (0-100 Hz) encompassing multi-resonance occurrence,

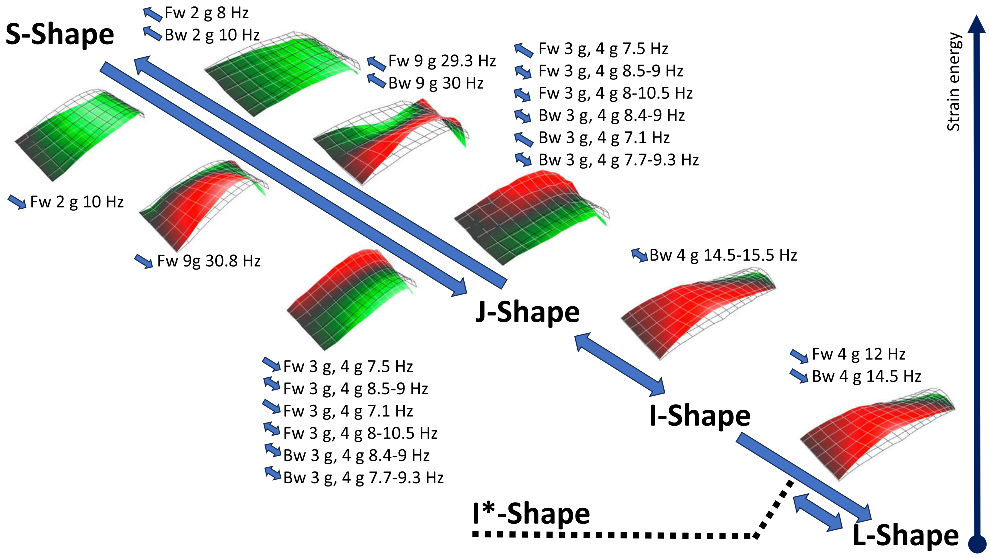

Fig. 23 Examined morphing transmission across stable equilibria for pentastable shell. Bidirectional arrows denote observed dynamics including both (or multiple) configurations, while unidirectional arrows represent one way jumps. Abbreviations Fw and Bw correspond to frequency forward and backward sweeps, respectively

nonlinear damping characteristics, and potential frequency ranges for dynamic configuration jump was discussed. For configurations **I**, **J**, **L** and **S**, an extensive experimental campaign explored the dynamic response to varying kinematic excitation magnitudes, as well as multiple resonances during frequency sweeps in both forward and backward directions. Rich in-well scenarios were presented, including hardening and softening phenomena, internal resonances with 1 : 2 and 2 : 1 ratios, and sub- and super-harmonic resonances with integer ratios of 2, 3 and 4. The comprehensive results of the cross-well and global dynamics are graphically summarized in Fig. 23. For selected resonance frequencies, a step test was conducted with incremental increases in excitation amplitude at a constant frequency. Based on this, parametric plots, phase portraits, and Poincaré maps were constructed and analyzed in terms of motion nature: (i) in-well, cross-well, and global dynamics, or (ii) periodic, quasi-periodic, and chaotic behavior. In selected cases, fast Fourier transforms and largest Lyapunov exponents were calculated to confirm the chaotic motion.

Being a pioneering work on pentastable composite shell its significant potential and dynamic behavior remain for further exploration and development. The complex dynamic responses observed suggest several directions for future work:

- Developing a reduced-order analytical model that incorporates geometric jump hysteresis to better predict the system's snap-through behavior [46];
- Investigating the system's nonlinear dynamic response using a tuned finite element model that captures configuration **I***;
- Designing and implementing comprehensive control mechanisms to regulate transitions between equilibrium states within the system;
- Study of fiber fatigue effects under prolonged operation to assess durability and performance over time;
- Conducting sensitivity analyses during the manufacturing process, particularly concerning thermomechanical parameters that impact the system's stability and performance.

Funding This research was funded in whole or in part by National Science Centre, Poland 2021/41/B/ST8/03190. For the purpose of Open Access, the author has applied a CC-BY public copyright licence to any Author Accepted Manuscript (AAM) version arising from this submission. DM declares support by NAWA STER Programme Internationalization of the Doctoral School of Lublin University of Technology - IDeaS of LUT. MB acknowledges the Italian National Group of Mathematical Physics INdAM-GNFM and the support from the Polytechnic

Department of Engineering and Architecture of the University of Udine through the project "ESPeRT".

Data availibility Enquiries about data availability should be directed to the authors.

Declarations

Conflict of interest The authors have not disclosed any competing interests.

References

1. Lu, S., He, Q., Wang, J.: A review of stochastic resonance in rotating machine fault detection. Mech. Syst. Signal Process. **116**, 230–260 (2019). https://doi.org/10.1016/j.ymssp.2018.06.032
2. Kim, P., Seok, J.: A multi-stable energy harvester: dynamic modeling and bifurcation analysis. J. Sound Vib. **333**(21), 5525–5547 (2014). https://doi.org/10.1016/j.jsv.2014.05.054
3. Hou, Z., Zha, W., Wang, H., Liao, W.-H., Bowen, C.R., Cao, J.: Bistable energy harvesting backpack: design, modeling, and experiments. Energy Convers. Manage. **259**, 115441 (2022). https://doi.org/10.1016/j.enconman.2022.115441
4. Lemos, D.M., Marques, F.D., Ferreira, A.J.M.: A review on bistable composite laminates for aerospace applications. Compos. Struct. **329**, 117756 (2024). https://doi.org/10.1016/j.compstruct.2023.117756
5. Mukherjee, A., Ali, S.F., Arockiarajan, A.: Hybrid bistable composite laminates for structural assemblies: a numerical and experimental study. Compos. Struct. **260**, 113467 (2021). https://doi.org/10.1016/j.compstruct.2020.113467
6. Lachenal, X., Weaver, P.M., Daynes, S.: Multi-stable composite twisting structure for morphing applications. Proc. R. Soc. A: Math., Phys. Eng. Sci. **468**(2141), 1230–1251 (2012). https://doi.org/10.1098/rspa.2011.0631
7. Librandi, G., Tubaldi, E., Bertoldi, K.: Programming nonreciprocity and reversibility in multistable mechanical metamaterials. Nat. Commun. (2021). https://doi.org/10.1038/s41467-021-23690-z
8. Gerson, Y., Krylov, S., Ilic, B., Schreiber, D.: Design considerations of a large-displacement multistable micro actuator with serially connected bistable elements. Finite Elem. Anal. Des. **49**(1), 58–69 (2012). https://doi.org/10.1016/j.finel.2011.08.021
9. Rechnitz, S., Tabachnik, T., Shlafman, M., Shlafman, S., Yaish, Y.E.: Mode coupling bi-stability and spectral broadening in buckled carbon nanotube mechanical resonators. Nat. Commun. (2022). https://doi.org/10.1038/s41467-022-33440-4
10. Fang, S., Zhou, S., Yurchenko, D., Yang, T., Liao, W.-H.: Multistability phenomenon in signal processing, energy harvesting, composite structures, and metamaterials: A review. Mech. Syst. Signal Process. **166**(4), 108419 (2022). https://doi.org/10.1016/j.ymssp.2021.108419
11. Hyer, M.W.: Some observations on the cured shape of thin unsymmetric laminates. J. Compos. Mater. **15**(2), 175–194 (1981). https://doi.org/10.1177/002199838101500207
12. Dai, F., Li, H., Du, S.: A multi-stable lattice structure and its snap-through behavior among multiple states. Compos. Struct. **97**(7), 56–63 (2013). https://doi.org/10.1016/j.compstruct.2012.10.016
13. Cui, Y., Santer, M.: Highly multistable composite surfaces. Compos. Struct. **124**(24), 44–54 (2015). https://doi.org/10.1016/j.compstruct.2014.12.052
14. Mostafavi, S., Golzar, M., Alibeigloo, A.: On the thermally induced multistability of connected curved composite plates. Compos. Struct. **139**, 210–219 (2016). https://doi.org/10.1016/j.compstruct.2015.12.006
15. Telford, R., Katnam, K.B., Young, T.M.: Analysing thermally induced macro-scale residual stresses in tailored morphing composite laminates. Compos. Struct. **117**(6), 40–50 (2014). https://doi.org/10.1016/j.compstruct.2014.06.013
16. Potter, K.D., Weaver, P.M.: A concept for the generation of out-of-plane distortion from tailored frp laminates. Compos. A Appl. Sci. Manuf. **35**(12), 1353–1361 (2004). https://doi.org/10.1016/j.compositesa.2004.06.022
17. Etches, J., Potter, K., Weaver, P., Bond, I.: Environmental effects on thermally induced multistability in unsymmetric composite laminates. Compos. A Appl. Sci. Manuf. **40**(8), 1240–1247 (2009). https://doi.org/10.1016/j.compositesa.2009.05.018
18. Brampton, C.J., Betts, D.N., Bowen, C.R., Kim, H.A.: Sensitivity of bistable laminates to uncertainties in material properties, geometry and environmental conditions. Compos. Struct. **102**(16–17), 276–286 (2013). https://doi.org/10.1016/j.compstruct.2013.03.005
19. Tuttle, M.E.: A mechanical/thermal analysis of prestressed composite laminates. J. Compos. Mater. **22**(8), 780–792 (1988). https://doi.org/10.1177/002199838802200806
20. Kebadze, E., Guest, S.D., Pellegrino, S.: Bistable prestressed shell structures. Int. J. Solids Struct. **41**(11–12), 2801–2820 (2004). https://doi.org/10.1016/j.ijsolstr.2004.01.028
21. Huang, D., Han, J., Zhou, S., Han, Q., Yang, G., Yurchenko, D.: Stochastic and deterministic responses of an asymmetric quad-stable energy harvester. Mech. Syst. Signal Process. **168**(6), 108672 (2022). https://doi.org/10.1016/j.ymssp.2021.108672
22. Zhou, Z., Qin, W., Yang, Y., Zhu, P.: Improving efficiency of energy harvesting by a novel penta-stable configuration. Sens. Actuators, A **265**(11), 297–305 (2017). https://doi.org/10.1016/j.sna.2017.08.039
23. Zhang, Z., Zhou, Y., Shen, H., Sun, M., Chai, H., Wu, H., Jiang, S.: Experimental study of orthogonal bistable laminated composite shell driven by magnetorheological elastomer. Compos. Struct. **271**(11), 114119 (2021). https://doi.org/10.1016/j.compstruct.2021.114119
24. Yang, T., Cao, Q., Li, Q., Qiu, H.: A multi-directional multistable device: modeling, experiment verification and applications. Mech. Syst. Signal Process. **146**, 106986 (2021). https://doi.org/10.1016/j.ymssp.2020.106986
25. Guest, S.D., Pellegrino, S.: Analytical models for bistable cylindrical shells. Proc. R. Soc. A: Math., Phys. Eng. Sci. **462**(2067), 839–854 (2006). https://doi.org/10.1098/rspa.2005.1598
26. Seffen, K.A.: 'morphing' bistable orthotropic elliptical shallow shells. Proc. R. Soc. A: Math., Phys. Eng. Sci. **463**(2077), 67–83 (2007). https://doi.org/10.1098/rspa.2006.1750

27. Cantera, M.A., Romera, J.M., Adarraga, I., Mujika, F.: Modelling and testing of the snap-through process of bi-stable cross-ply composites. Compos. Struct. **120**(2), 41–52 (2015). https://doi.org/10.1016/j.compstruct.2014.09.064
28. Wu, M.Q., Zhang, W., Chronopoulos, D.: Nonlinear vibrations and dynamic snap-through behaviors of four-corner simply supported bistable asymmetric laminated composite square shell. Mech. Syst. Signal Process. **173**(1), 109023 (2022). https://doi.org/10.1016/j.ymssp.2022.109023
29. Arrieta, A.F., Spelsberg-Korspeter, G., Hagedorn, P., Neild, S.A., Wagg, D.J.: Low order model for the dynamics of bi-stable composite plates. J. Intell. Mater. Syst. Struct. **22**(17), 2025–2043 (2011). https://doi.org/10.1177/1045389X11422104
30. Liu, T., Zhang, W., Zheng, Y., Zhang, Y.F., Zhao, W.: Potential well evolution and metastable dynamics of bistable asymmetric laminated composite square shallow shell under external and parametric excitations. Compos. Struct. **280**(2), 114936 (2022). https://doi.org/10.1016/j.compstruct.2021.114936
31. Coburn, B.H., Pirrera, A., Weaver, P.M., Vidoli, S.: Tristability of an orthotropic doubly curved shell. Compos. Struct. **96**(2), 446–454 (2013). https://doi.org/10.1016/j.compstruct.2012.08.026
32. Vidoli, S., Maurini, C.: Tristability of thin orthotropic shells with uniform initial curvature. Proc. R. Soc. A: Math., Phys. Eng. Sci. **464**(2099), 2949–2966 (2008). https://doi.org/10.1098/rspa.2008.0094
33. Algmuni, A., Xi, F., Alighanbari, H.: Design and analysis of a grid patch multi-stable composite. Compos. Struct. **246**(2), 112378 (2020). https://doi.org/10.1016/j.compstruct.2020.112378
34. Chillara, V.S.C., Dapino, M.J.: Bistable laminates with non-cylindrical curved shapes. Compos. Struct. **230**(6), 111502 (2019). https://doi.org/10.1016/j.compstruct.2019.111502
35. Arrieta, A.F., Kuder, I.K., Waeber, T., Ermanni, P.: Variable stiffness characteristics of embeddable multi-stable composites. Compos. Sci. Technol. **97**(9), 12–18 (2014). https://doi.org/10.1016/j.compscitech.2014.03.017
36. Brunetti, M., Vincenti, A., Vidoli, S.: A class of morphing shell structures satisfying clamped boundary conditions. Int. J. Solids Struct. **82**(6), 47–55 (2016). https://doi.org/10.1016/j.ijsolstr.2015.12.017
37. Brunetti, M., Kloda, L., Romeo, F., Warminski, J.: Multistable cantilever shells: analytical prediction, numerical simulation and experimental validation. Compos. Sci. Technol. **165**(14), 397–410 (2018). https://doi.org/10.1016/j.compscitech.2018.06.021
38. Brunetti, M., Vidoli, S., Vincenti, A.: Bistability of orthotropic shells with clamped boundary conditions: An analysis by the polar method. Compos. Struct. **194**(9), 388–397 (2018). https://doi.org/10.1016/j.compstruct.2018.04.009
39. Brunetti, M., Mitura, A., Romeo, F., Warminski, J.: Nonlinear dynamics of bistable composite cantilever shells: an experimental and modelling study. J. Sound Vib. **526**(2), 116779 (2022). https://doi.org/10.1016/j.jsv.2022.116779
40. Mitura, A., Brunetti, M., Kloda, L., Romeo, F., Warminski, J.: Experimental nonlinear dynamic regimes for energy harvesting from cantilever bistable shells. Mech. Syst. Signal Process. **206**(9), 110890 (2024). https://doi.org/10.1016/j.ymssp.2023.110890
41. Walker, S.J.I., Aglietti, G.S.: A study of tape spring fold curvature for space deployable structures. Proc. Inst. Mech. Eng., Part G: J. Aerosp. Eng. **221**(3), 313–325 (2007). https://doi.org/10.1243/09544100JAERO209
42. Coppedè, M., Paroni, R., Picchi Scardaoni, M.: Numerical investigation of the asymptotic behavior of tape springs. J. Theor. Appl. Mech. (2024). https://doi.org/10.15632/jtam-pl/189814
43. Luongo, A., Leamy, M.J., Lenci, S., Piccardo, G., Touzé, C.: Advances in stability, bifurcations and nonlinear vibrations in mechanical systems. Nonlinear Dyn. **103**(4), 2993–2995 (2021). https://doi.org/10.1007/s11071-021-06404-4
44. Lenci, S., Clementi, F., Kloda, L., Warminski, J., Rega, G.: Longitudinal-transversal internal resonances in timoshenko beams with an axial elastic boundary condition. Nonlinear Dyn. **103**(4), 3489–3513 (2021). https://doi.org/10.1007/s11071-020-05912-z
45. Kodba, S., Perc, M., Marhl, M.: Detecting chaos from a time series. Eur. J. Phys. **26**(1), 205–215 (2005). https://doi.org/10.1088/0143-0807/26/1/021
46. Luongo, A., Casciati, S., Zulli, D.: Perturbation method for the dynamic analysis of a bistable oscillator under slow harmonic excitation. Smart Struct. Syst. **18**(1), 183–196 (2016). https://doi.org/10.12989/sss.2016.18.1.183